Performances of a family of new sequential Bayesian filters for input estimation

Julian Ghibaudo, Mathieu Aucejo, Olivier de Smet

Performances of a family of new sequential Bayesian filters for input estimation

J. Ghibaudo, M. Aucejo and O. De Smet[a]

[a]*Laboratoire de Mécanique des Structures et des Systèmes Couplés, Conservatoire National des Arts et Métiers, 75003 Paris, France, HESAM Université*

Abstract

During their lifetime, structures are usually subjected to some mechanical shocks that generate high levels of vibration that can damage the structure itself as well as the embedded devices. However, the characteristics of these shocks (location, time history, maximum intensity, ...) are often unknown due to the inaccessibility of the excitation region for direct force measurements or the inability to instrument the system. Therefore, inverse methods have been developed to quantify these complex excitations. Recently, a Bayesian formulation of the input-state estimation problem for linear systems has been proposed by the authors, which unifies most of the state-of-the-art filters. In this paper, we present two novel Bayesian filters derived from this framework: (a) the Correlated Dual Kalman Filter (CDKF), which is one of the filters that naturally follows from the unified Bayesian formulation, and (b) the Component Bayesian Filter (CBF), which promotes spatial sparsity of the input vector. Essentially, these filters differ in the prior distributions used to convey information about the spatial distribution of the input vector to be identified. The performance of these filters is evaluated through a

*Corresponding author. E-mail address: mathieu.aucejo@lecnam.net

numerical experiment and a real-world application aimed at reconstructing a sparse and transient excitation acting on a linear structure. A comparison of these original filters with other Bayesian filters proposed in the literature is also proposed. In particular, the numerical experiment allows to study the performance of the proposed filters in different scenarios, such as the number of sensors, the measurement noise level or the sensor configuration, while the real-world application allows to test them in operational conditions. More specifically, it is shown that filters promoting the spatial sparsity of the input vector, such as CBF, lead to a consistent identified excitation profile when acceleration measurements are the only available data.
Keywords: Linear inverse problem, Force localization, Space-time approach, Bayesian filter, Kalman filter.

1. Introduction

Force identification is a recurring topic in structural dynamics due to the lack of knowledge of the mechanical excitations acting on a structure, which is one of the prerequisites to improve its design, monitor its performance or increase its lifetime. For example, a mechanical shock, whether intentional or not, can damage structures and cause integrated equipment to fail, which can interrupt operations. However, the actual impact is usually difficult to characterize due to the difficulty of instrumenting the area of interest with force sensors or the lack of knowledge of its space-time characteristics (location, duration and intensity). These practical considerations make it necessary to implement inverse identification methods to estimate the sources of excitation from the measurement of kinematic quantities (strain, displacement,

velocity or acceleration). Unfortunately, this inverse problem is mathematically ill-posed and leads to significant reconstruction errors when solved in a naive manner.

For time-domain applications, this negative side effect has been addressed by the development of specific solution strategies [1–9], especially in the case of linear systems. Among all the existing methods in the literature, the most widely used are Tikhonov-like regularization and Kalman-like filtering. These two approaches were developed in the early 1960's in the respective works of Andrey Tikhonov [10] and Rudolf Kalman [11]. Despite some obvious differences, they still share some common features. First, the Kalman gain can be viewed as an inverse regularization operator, similar to the one defined by Tikhonov. Second, both methods can be derived from the Bayesian formalism [12, 13], which provides a better understanding of the main assumptions underlying these strategies and opens the way to new developments and analyses. More precisely, Tikhonov-like regularization is a particular type of Bayesian regularization, while Kalman-like filters belong to the general class of Bayesian filters. Whereas Tikhonov-like regularization is generally performed on the whole set of measurements, Kalman-like filtering solves the inverse problem recursively, using a prediction/estimation scheme at each time step. As it is recursive, faster and computationally cheaper than the regularization, it has been widely developed. Several filters have been proposed in the literature to solve the input-state estimation problem for linear systems. They can be divided into two types: the joint filters and the sequential ones. Here, the joint filters refer to Bayesian filters within which the estimations of both the state and the input vectors are made together, in

the same computation step, as opposed to the sequential ones, where these estimations are made one after another, successively. In fact, the joint filters aggregate the filters where an augmented state including the input is generated, as the Augmented Kalman Filter (AKF) of Lourens et al. [14] or the filters based on a Gaussian Process Latent Force Model [15, 16]. The sequential filters include the one developed by Gillijns and De Moor (GDF) [17, 18], the Sequential Bayesian Filter (SBF) developed by Sedehi et al. [19] or the Dual Kalman Filter (DKF) proposed by Eftekhar Azam et al. [20], where state estimation and input estimation compete in the same time step. Although some prior information about the spatial distribution of the input vector is introduced in the literature examples, it often does not sufficiently constrain the resulting estimates. Thus, despite the reasonable performance of these filters, it induces errors in the identification of the excitation field when the mechanical sources are spatially sparse and transient. Therefore, when only acceleration measurements are used for the input estimation, a drift effect appears in several state-of-the-art filters, which increases the global reconstruction error and quickly makes these filters inaccurate online [21]. To counterbalance this aspect, the authors introduced the Sparse adaptive Bayesian Filter (SaBF), in which a generalized Gaussian distribution over the input vector is assumed during the prediction step [21]. This original filter avoids the drift effect and promotes the spatial sparsity of the force to be identified, while remaining purely recursive. The proposed approach to address this challenge is based on a Bayesian formulation of the problem of estimating both the input and the state vectors in a sequential manner. Inspired by the work of Sedehi et al. [19], it unifies most of the state-of-the-art

filters under the same Bayesian formulation [21].
Finally, although it is beyond the scope of this paper, which focuses on the force identification problem and is limited to linear Bayesian filtering, it is worth mentioning some extensions related to input-state-parameter estimation problems in order to give the reader a better overview of the advances in the field. This kind of problems generally leads to a nonlinear filtering process for which an Extended Kalman Filter [22–25] or an Unscented Kalman Filter [26, 27] is usually implemented to solve the nonlinear part of the formulation.

In the present paper, two original sequential filters derived from the aforementioned unified Bayesian vision are presented, although they are widely influenced by the literature. First, a generalization of the predictive distribution over the input proposed in SBF combined with the relaxation of some assumptions made in DKF, leads to the Correlated Dual Kalman Filter (CDKF), in which the state and input vectors are estimated sequentially but not independently as in DKF. Then, based on the same formalism, an alternative version of SaBF, called Component Bayesian Filter (CBF), is introduced. In this formulation, the components of the input vector are assumed to be independent and to follow a generalized Gaussian distribution. Here, all the hyperparameters are automatically selected from a Bayesian optimization that estimates at each time step their most probable value given the available data. In order to properly introduce the two proposed linear Bayesian filters and to highlight their originality with respect to the existing literature, the present paper is divided into five parts. Sections 2 and 3 are dedicated to the definition of the state-space representation used throughout

the paper, as well as a reminder of the unified Bayesian formulation of the sequential state-input estimation problem. Section 4 focuses on the derivation of CDKF and CBF, which belong to a larger family of sequential Bayesian filters. Finally, sections 5 and 6 set up a numerical experiment and a real-world application to evaluate the validity of the proposed approaches for the reconstruction of a hammer impact based on acceleration measurements. Their relative performances in terms of peak reconstruction, input location and appearance of the drift phenomenon are compared with each other and with AKF. It is shown that SaBF and the proposed CBF strategies provide better results in terms of input estimation accuracy by avoiding the drift effect. CDKF brings a slight improvement over AKF by reducing the global drift deviation.

2. Discretized state-space representation of dynamical systems

Bayesian filtering is based on the state-space representation of the dynamical system of interest. Here, only time-invariant linear mechanical systems are considered. Formally, this implies that the discretized state-space representation can be expressed in the following generic form:

$$\begin{cases} \mathbf{x}_{k+1} = \mathbf{A}\mathbf{x}_k + \mathbf{B}\mathbf{u}_k + \mathbf{w}_k^{\mathbf{x}} \\ \mathbf{y}_k = \mathbf{C}\mathbf{x}_k + \mathbf{D}\mathbf{u}_k + \mathbf{v}_k \end{cases}, \tag{1}$$

where $\mathbf{x}_k$, $\mathbf{u}_k$ and $\mathbf{y}_k$ are the state, input and output vectors at time step k, while $\mathbf{A}$, $\mathbf{B}$, $\mathbf{C}$ and $\mathbf{D}$ are, respectively, the constant discretized state, input, output and feedthrough matrices. Here, $\mathbf{w}_k^{\mathbf{x}}$ denotes the Gaussian process noise with zero mean and covariance matrix $\mathbf{Q}_k^{\mathbf{x}}$ and $\mathbf{v}_k$ is the Gaussian mea-

surement noise with zero mean and covariance matrix $\mathbf{R}_k$.

From a Bayesian perspective, the previous discretized state-space representation can be expressed as [13]:

$$\begin{cases} \mathbf{x}_{k+1} \sim p(\mathbf{x}_{k+1}|\mathbf{x}_k, \mathbf{u}_k) = \mathcal{N}(\mathbf{x}_{k+1}|\mathbf{A}\mathbf{x}_k + \mathbf{B}\mathbf{u}_k, \mathbf{Q}_k^{\mathbf{x}}) \\ \mathbf{y}_k \sim p(\mathbf{y}_k|\mathbf{x}_k, \mathbf{u}_k) = \mathcal{N}(\mathbf{y}_k|\mathbf{C}\mathbf{x}_k + \mathbf{D}\mathbf{u}_k, \mathbf{R}_k) \end{cases}, \tag{2}$$

where $\mathcal{N}(\mathbf{x}|\boldsymbol{\mu}, \boldsymbol{\Sigma})$ is the multivariate normal distribution with mean $\boldsymbol{\mu}$ and covariance matrix $\boldsymbol{\Sigma}$ associated to the random vector $\mathbf{x}$.

3. Bayesian formulation of the sequential input-state estimation problem

This section briefly recalls the unified Bayesian formulation of the sequential state-input estimation problem in order to make the paper self-sufficient. In this formulation, inspired by the work of Sedehi et al. [19] and further developed by the authors in [21], the state vector $\mathbf{x}_k$ and the input vector $\mathbf{u}_k$ are computed sequentially, meaning that these two estimations are correlated as the next one needs the previous one to be estimated.
From a general point of view, the unified Bayesian approach to the sequential estimation of the input and state vectors can be divided into the following five steps (interested readers can refer to Ref. [21] for further details):

1. Initialization at $k = 0$

   The initialization of the input and state vectors consists in defining the prior probability distributions over the initial input vector, $\mathbf{u}_0$, and the

initial state vector, $\mathbf{x}_0$. Here, these prior probability distributions are defined as follows:

$$p(\mathbf{u}_0) = \mathcal{N}(\mathbf{u}_0|\widehat{\mathbf{u}}_0, \mathbf{P}_0^{\mathbf{u}}) \text{ and } p(\mathbf{x}_0) = \mathcal{N}(\mathbf{x}_0|\widehat{\mathbf{x}}_0, \mathbf{P}_0^{\mathbf{x}}), \tag{3}$$

where the mean vectors, $\widehat{\mathbf{u}}_0$ and $\widehat{\mathbf{x}}_0$, and the covariance matrices, $\mathbf{P}_0^{\mathbf{u}}$ and $\mathbf{P}_0^{\mathbf{x}}$, are known quantities. To complete the initialization step, one has to compute the predictive distribution $p(\mathbf{x}_1|\mathbf{y}_0)$, assuming that the initial vectors are statistically independent :

$$p(\mathbf{x}_1|\mathbf{y}_0) = \mathcal{N}(\mathbf{x}_1|\widetilde{\mathbf{x}}_1, \widetilde{\mathbf{P}}_1^{\mathbf{x}}), \tag{4}$$

where $\widetilde{\mathbf{x}}_1 = \mathbf{A}\widehat{\mathbf{x}}_0 + \mathbf{B}\widehat{\mathbf{u}}_0$ is the predicted state and $\widetilde{\mathbf{P}}_1^{\mathbf{x}} = \mathbf{A}\mathbf{P}_0^{\mathbf{x}}\mathbf{A}^{\mathsf{T}} + \mathbf{B}\mathbf{P}_0^{\mathbf{u}}\mathbf{B}^{\mathsf{T}} + \mathbf{Q}_0$, its covariance matrix.

2. Prediction of the input vectors at time step k

   To make a prediction of the input vector, the predictive distribution $p(\mathbf{u}_k|\mathbf{y}_{1:k-1})$ must be defined. If no assumptions are made about the spatial distribution of the input vector, this distribution is unknown. Existing sequential filters typically differ at this stage. To make the proposed Bayesian filter more general and applicable to a wider range of literature, it is assumed without any simplification that the probability distribution is a multivariate Gaussian law with a mean and covariance matrix $\widetilde{\mathbf{u}}_k$ and covariance matrix $\widetilde{\mathbf{P}}_k^{\mathbf{u}}$, that is:

$$p(\mathbf{u}_k|\mathbf{y}_{1:k-1}) = \mathcal{N}(\mathbf{u}_k|\widetilde{\mathbf{u}}_k, \widetilde{\mathbf{P}}_k^{\mathbf{u}}). \tag{5}$$

3. Estimation of the input vectors at time step k

The estimation of the input vector requires the filtering probability distribution $p(\mathbf{u}_k|\mathbf{y}_{1:k})$. By applying the Bayes' rule to $p(\mathbf{u}_k|\mathbf{x}_k, \mathbf{y}_{1:k})$ and marginalizing the results over $\mathbf{x}_k$, the filtering probability distribution over the input vector becomes:

$$p(\mathbf{u}_k|\mathbf{y}_{1:k}) = \mathcal{N}(\mathbf{u}_k|\widehat{\mathbf{u}}_k, \mathbf{P}_k^{\mathbf{u}}), \tag{6}$$

where

$$\widehat{\mathbf{u}}_k = \widetilde{\mathbf{u}}_k + \mathbf{K}_k^{\mathbf{u}}\,\mathbf{i}_k^{\mathbf{u}}, \tag{7a}$$

$$\mathbf{P}_k^{\mathbf{u}} = (\mathbf{I} - \mathbf{K}_k^{\mathbf{u}}\mathbf{D})\widetilde{\mathbf{P}}_k^{\mathbf{u}} + \mathbf{K}_k^{\mathbf{u}}\mathbf{C}\widetilde{\mathbf{P}}_k^{\mathbf{x}}\mathbf{C}^{\mathsf{T}}\mathbf{K}_k^{\mathbf{u}\mathsf{T}}, \tag{7b}$$

$$\mathbf{K}_k^{\mathbf{u}} = \widetilde{\mathbf{P}}_k^{\mathbf{u}}\mathbf{D}^{\mathsf{T}}(\mathbf{D}\widetilde{\mathbf{P}}_k^{\mathbf{u}}\mathbf{D}^{\mathsf{T}} + \mathbf{R}_k)^{-1}, \tag{7c}$$

$$\mathbf{i}_k^{\mathbf{u}} = \mathbf{y}_k - \mathbf{C}\widetilde{\mathbf{x}}_k - \mathbf{D}\widetilde{\mathbf{u}}_k. \tag{7d}$$

4. Estimation of the state vector at time step k

   As for the input vector, the estimation of the state vector requires the filtering probability distribution $p(\mathbf{x}_k|\mathbf{y}_{1:k})$, corresponding to the following marginal distribution:

$$p(\mathbf{x}_k|\mathbf{y}_{1:k}) = \mathcal{N}(\mathbf{x}_k|\widehat{\mathbf{x}}_k, \mathbf{P}_k^{\mathbf{x}}), \tag{8}$$

   where

$$\widehat{\mathbf{x}}_k = \widetilde{\mathbf{x}}_k + \mathbf{K}_k^{\mathbf{x}}\,\mathbf{i}_k^{\mathbf{x}}, \tag{9a}$$

$$\mathbf{P}_k^{\mathbf{x}} = (\mathbf{I} - \mathbf{K}_k^{\mathbf{x}}\mathbf{C})\widetilde{\mathbf{P}}_k^{\mathbf{x}} + \mathbf{K}_k^{\mathbf{x}}\mathbf{D}\mathbf{P}_k^{\mathbf{u}}\mathbf{D}^{\mathsf{T}}\mathbf{K}_k^{\mathbf{x}\mathsf{T}}, \tag{9b}$$

$$\mathbf{K}_k^{\mathbf{x}} = \widetilde{\mathbf{P}}_k^{\mathbf{x}}\mathbf{C}^{\mathsf{T}}(\mathbf{C}\widetilde{\mathbf{P}}_k^{\mathbf{x}}\mathbf{C}^{\mathsf{T}} + \mathbf{R}_k)^{-1}, \tag{9c}$$

$$\mathbf{i}_k^{\mathbf{x}} = \mathbf{y}_k - \mathbf{C}\widetilde{\mathbf{x}}_k - \mathbf{D}\widehat{\mathbf{u}}_k. \tag{9d}$$

At this stage, it is possible to compute the cross-covariance matrix $\mathbf{P}_k^{\mathbf{xu}}$:

$$\mathbf{P}_k^{\mathbf{xu}} = \mathbb{E}\left[(\mathbf{x}_k - \widehat{\mathbf{x}}_k)(\mathbf{u}_k - \widehat{\mathbf{u}}_k)^{\mathsf{T}}\right] = -\mathbf{K}_k^{\mathbf{x}}\mathbf{D}\mathbf{P}_k^{\mathbf{u}}. \tag{10}$$

where $\mathbb{E}(\mathbf{x})$ is the expected value of the random vector $\mathbf{x}$.

5. Prediction of the state vector at time step $k+1$

   The last step of the sequential Bayesian Filter is the computation of the predictive distribution over the state vector at time step $k+1$ to continue the recursive process:

$$p(\mathbf{x}_{k+1}|\mathbf{y}_{1:k}) = \mathcal{N}(\mathbf{x}_{k+1}|\widetilde{\mathbf{x}}_{k+1}, \widetilde{\mathbf{P}}_{k+1}^{\mathbf{x}}), \tag{11}$$

   where

$$\widetilde{\mathbf{x}}_{k+1} = \mathbf{A}\widehat{\mathbf{x}}_k + \mathbf{B}\widehat{\mathbf{u}}_k, \tag{12a}$$

$$\widetilde{\mathbf{P}}_{k+1}^{\mathbf{x}} = \begin{bmatrix}\mathbf{A} & \mathbf{B}\end{bmatrix} \begin{bmatrix}\mathbf{P}_k^{\mathbf{x}} & \mathbf{P}_k^{\mathbf{xu}} \\ \mathbf{P}_k^{\mathbf{xu}\mathsf{T}} & \mathbf{P}_k^{\mathbf{u}}\end{bmatrix} \begin{bmatrix}\mathbf{A}^{\mathsf{T}} \\ \mathbf{B}^{\mathsf{T}}\end{bmatrix} + \mathbf{Q}_k. \tag{12b}$$

This general Bayesian formulation allows to obtain the sequential filters existing in the literature, namely GDF, SBF and DKF, by modifying the general hypotheses made on the choice of the predictive distribution (see step 2). The various assumptions used for deriving a particular filter will not be developed here, but explanations are available in Ref. [21]. However, it can be stated here that these filters behave quite similarly when identifying transient sparse sources from a dense array of acceleration measurements, especially with respect to the well-known drift effect.

4. Development of a new family of Sequential Bayesian Filters

The previous section described the general formulation of the sequential input-state estimation problem. This formulation allows to retrieve most of the existing state-of-the-art filters. More precisely, the proposed Bayesian formalism shows that existing Kalman-like sequential filters use different assumptions to define the predictive probability distribution over the input vector $p(\mathbf{u}_k|\mathbf{y}_{1:k-1})$. This observation is the main motivation behind the proposed family of sequential Bayesian filters, which aim to incorporate prior information about the spatial distribution of the input vector into the formulation during the prediction step. Here, the predictive probability distribution is chosen to add a restrictive constraint on the shape of the input. This addition has the effect of forcing the estimation to take into account our prior knowledge of the sources to be identified. The different hypotheses as well as their influence on the implementation are developed here after.

4.1. Correlated Dual Kalman Filter – CDKF

This filter follows naturally from the unified Bayesian formulation recalled in section 3, since it mainly consists in directly specifying the mean vector and the covariance matrix of the predictive distribution defined in Eq. (5) of step 2. To do so, a fictitious equation is added to the state-space representation of the Eq. (1) on the input vector, so that the input vector is following a random walk as for AKF and DKF, that is:

$$\mathbf{u}_{k+1} = \mathbf{u}_k + \mathbf{w}_k^{\mathbf{u}}, \tag{13}$$

Hence a new hypothesis on the input model is done, as the variable follows a Gaussian distribution with mean $\mathbf{u}_k$ and a to-be-determined covariance $\mathbf{Q}_k^{\mathbf{u}}$,

associated the process noise $\mathbf{w}_k^{\mathbf{u}}$. In practice, this covariance matrix is chosen to be isotropic, meaning that only a single variance parameter, σ_u^2, has to be estimated [14, 20]. As for SBF, the methodology developed in section 3 is perfectly followed for the implementation of this filter. Thus, the predictive distribution becomes:

$$p(\mathbf{u}_k|\mathbf{y}_{1:k-1}) = \mathcal{N}(\mathbf{u}_k|\widetilde{\mathbf{u}}_k, \widetilde{\mathbf{P}}_k^{\mathbf{u}}) = \mathcal{N}(\widetilde{\mathbf{u}}_k|\widehat{\mathbf{u}}_{k-1}, \mathbf{Q}_{k-1}^{\mathbf{u}} + \mathbf{P}_{k-1}^{\mathbf{u}}) \tag{14}$$

Except for this minor change, all of the equations defined in steps 3 to 5 remain unchanged. Compared to SBF, the mean of this prior distribution is no longer the zero vector, while the predictive covariance matrix is also changed, with the addition of noise covariance matrix $\mathbf{Q}_{k-1}^{\mathbf{u}}$. Furthermore, unlike DKF[1], CDKF preserves the cross-correlation between the state and input vectors, making their estimation coupled. In this sense, CDKF can seen as a generalization or an hybrid of SBF and DKF.

4.2. Sparse Adaptive Bayesian Filter – SaBF

Since the SaBF has been fully introduced by the authors in their own paper [21], only the basic equations and principles will be recalled here. This remainder is proposed for pedagogical purposes and to highlight the connection of this filter with the Component Bayesian Filter introduced in the next section.

For SaBF, the choice of the predictive probability distribution aims at promoting either the sparsity or the smoothness of the spatial distribution

[1]For further information about the assumptions used for deriving DKF, the reader can refer to Ref. [21]

of the input vector. This requirement leads us to choose a multivariate generalized Gaussian distribution with zero mean:

$$\begin{aligned} p(\mathbf{u}_k|\mathbf{y}_{1:k-1}) &= \mathcal{N}_g(\mathbf{u}_k|\mathbf{0}, \tau_k, q_k) \\ &= \left(\frac{q_k^{1-\frac{1}{q_k}}}{2\Gamma(\frac{1}{q_k})} \right)^{N_u} \tau_k^{\frac{N_u}{q_k}} \exp\left(-\frac{\tau_k}{q_k} \|\mathbf{u}_k\|_{q_k}^{q_k} \right), \end{aligned} \tag{15}$$

with $q_k \in \mathbb{R}^{+*}$, the shape parameter of the distribution at the time step k; $\| \bullet \|_q$, the ℓ_q-norm ($q \geq 1$) or quasi-norm ($q < 1$); τ_k, the scale parameter of the distribution at the time step k; N_u, the number of components of the input vector; $\Gamma(x)$, the gamma function.

It is worth mentioning here that the choice of the previous multivariate Gaussian distribution offers some flexibility for encoding one's prior knowledge of the spatial distribution of the input vector, since it allows enforcing the sparsity of the input vector when $q_k \leq 1$ or its smoothness when $q_k \geq 2$ [28].

To comply with the Bayesian formulation presented in section 3, the following Gaussian approximation is used [29]:

$$\mathcal{N}_g(\mathbf{u}_k|\mathbf{0}, \tau_k, q_k) \propto \mathcal{N}(\mathbf{u}_k|\mathbf{0}, \mathbf{W}_k^{-1}/\tau_k). \tag{16}$$

This relation is valid for a suitable choice of the scale and shape parameters (τ_k, q_k) and the matrix $\mathbf{W}_k$. This matrix has to satisfy the Mercer's conditions (positive, definite, symmetric).

From this proposed predictive distribution and the previous equation, the estimation becomes:

$$\widehat{\mathbf{u}}_k = (\mathbf{D}\mathbf{R}_k^{-1}\mathbf{D}^\mathsf{T} + \tau_k\mathbf{W}_k)^{-1}\mathbf{D}^\mathsf{T}\mathbf{R}_k^{-1}\,\mathbf{i}_k^{\mathbf{u}}, \tag{17}$$

where $\mathbf{i}_k^{\mathbf{u}} = \mathbf{y}_k - \mathbf{C}\widetilde{\mathbf{x}}_k$ is the innovation vector.

The latter equation allows identifying the Kalman gain $\mathbf{K}_k^{\mathbf{u}}$ and the predictive covariance matrix $\widetilde{\mathbf{P}}_k^{\mathbf{u}}$ as:

$$\mathbf{K}_k^{\mathbf{u}} = (\mathbf{D}\mathbf{R}_k^{-1}\mathbf{D}^\mathsf{T} + \tau_k\mathbf{W}_k)^{-1}\mathbf{D}^\mathsf{T}\mathbf{R}_k^{-1} \quad \text{and} \quad \widetilde{\mathbf{P}}_k^{\mathbf{u}} = (\tau_k\mathbf{W}_k)^{-1}. \tag{18}$$

The hyperparameters q_k, τ_k and $\mathbf{W}_k$ are computed following a nested Bayesian optimization, which leads to the most probable values of all the parameters of the problem, resulting in $\widehat{\mathbf{u}}_k$ and the corresponding covariance matrix $\widehat{\mathbf{P}}_k^{\mathbf{u}}$. All expressions and ideas are given in [21].

4.3. Component Bayesian Filter – CBF

Like SaBF, CBF aims to promote spatial sparsity in the input vector. However, unlike SaBF, the idea here is to operate in a component-wise fashion, assuming that each component of the input vector is independent and follows a univariate generalized Gaussian distribution with zero mean and precision parameter τ_{ki}. Consequently, the predictive distribution over the input vector is such that:

$$\begin{aligned} p(\mathbf{u}_k|\mathbf{y}_{1:k-1}) &= \prod_{i=1}^{N_u} \mathcal{N}_g(u_{ki}|0,\tau_{ki},q_k) \\ &= \left(\frac{q_k^{\,1-\frac{1}{q_k}}}{2\Gamma(\frac{1}{q_k})}\right)^{N_u} \prod_{i=1}^{N_u} {\tau_{ki}}^{\frac{1}{q_k}} \exp\left(-\frac{\tau_{ki}}{q_k}|u_{ki}|^{q_k}\right). \end{aligned} \tag{19}$$

In doing so, it is expected to have a greater flexibility than for SaBF in selecting of the hyperparameters of the problem and thus a better reconstruction accuracy, but at the cost of an increase in the number of hyperparameters to estimate.

Thus, the idea of SaBF is duplicated N_u times and the computation of the optimal values is performed similarly by a dedicated Bayesian optimization, which aims to identify the most probable values of all the parameters involved in the problem at each time step, given the available data. One of the goals of this optimization procedure is to determine the scale and shape parameters (τ_{ki}, q_k) and the matrix $\mathbf{W}_k$ that best fit the Gaussian approximation defined as:

$$\prod_{i=1}^{N_u} \mathcal{N}_g(u_{ki}|0, \tau_{ki}, q_k) \propto \mathcal{N}(\mathbf{u}_k|\mathbf{0}, (\mathbf{T}_k\mathbf{W}_k)^{-1}), \tag{20}$$

with $\mathbf{T}_k = \text{diag}(\tau_{k1}, \ldots, \tau_{kN_u})$, in order to comply with the Bayesian formulation presented in section 3.

Like SaBF, the Bayesian optimization procedure consists in computing the Maximum A Posteriori (MAP) estimator of the following posterior probability distribution:

$$\begin{aligned}(\widehat{\mathbf{u}}_k, \widehat{\tau}_{ki}, \widehat{q}_k) &= \underset{(\mathbf{u}_k, \tau_{ki}, q_k)}{\text{argmax}}\ p(\mathbf{u}_k, \tau_{ki}, q_k|\mathbf{i}_k^{\mathbf{u}}) \\ &= \underset{(\mathbf{u}_k, \tau_{ki}, q_k)}{\text{argmax}}\ p(\mathbf{i}_k^{\mathbf{u}}|\mathbf{u}_k)\, p(\mathbf{u}_k|\tau_{ki}, q_k)\, p(\tau_{ki})\, p(q_k),\end{aligned} \tag{21}$$

where the prior distribution $p(\mathbf{u}_k|\tau_{ki}, q_k) = p(\mathbf{u}_k|\mathbf{y}_{1:k-1})$. All the calculations are not developed in this paper for reasons of brevity, but some elements are given below. Interested readers may refer to Ref. [21] for further details.

The solution of the previous optimization problem is obtained by maximizing the full conditional probability distributions associated to each parameter. However, the prior probability distribution over the scale and shape parameters, τ_k and q_k, and the likelihood function $p(\mathbf{i}_k^{\mathbf{u}}|\mathbf{u}_k)$ remain to be specified. These probability distributions are the same as for SaBF [21], i.e. a Gamma distribution for the scale parameter τ_{ki} and a truncated inverse Gamma distribution for the shape parameter q_k in the interval $]0, 2]$, as expressed in the following equations:

$$\begin{aligned} \mathcal{G}(\tau_k|\alpha_t, \beta_t) &= \frac{\beta_t^{\alpha_t}}{\Gamma(\alpha_t)} \tau_t^{\alpha_t - 1} \exp(-\beta_t \tau_k), \\ \mathcal{IG}_T(q_k|\alpha_q, \beta_q) &= \frac{\beta_q^{\alpha_q}}{\Gamma(\alpha_q)} (1/q_k)^{\alpha_q + 1} \exp(-\beta_q/q_k) \mathbb{I}_{[l_b, u_b]}(q_k), \end{aligned} \tag{22}$$

where $\mathbb{I}_{[l_b, u_b]}(q_k)$ is the truncation function on the interval $[l_b, u_b]$, α_t and β_t are respectively the scale parameter and the rate parameters of the Gamma distribution, while α_q and β_q are respectively the scale parameter and the rate parameter of the inverse Gamma distribution. To avoid biasing the estimation, one sets $\alpha_t = \alpha_q = 1$ and $\beta_t = \beta_q = 10^{-18}$. In addition, even if q_k is given in the interval $]0, 2]$, its true value is only approximately known. To translate this information into mathematical terms, $(l_b, u_b) = (0.01, 2)$.

Practically, as the full conditional probability distributions are available, the solution of the previous optimization problem can be computed by solving

iteratively the optimization subproblems defined by Eq. (23):

$$\widehat{\tau}_{ki} = \underset{q_k}{\operatorname{argmin}} \left(\beta_t + \frac{|u_{ki}|^{q_k}}{q_k}\right) \tau_{ki} + \left(1 - \alpha_t - \frac{1}{q_k}\right) \log \tau_{ki}, \tag{23a}$$

$$\widehat{q}_k = \underset{q_k}{\operatorname{argmin}}\ f(q_k|\mathbf{u}_k, \tau_{ki}), \tag{23b}$$

$$\widehat{\mathbf{u}}_k = \underset{\mathbf{u}_k}{\operatorname{argmin}} \frac{1}{2}\|\mathbf{i}_k^{\mathbf{u}} - \mathbf{D}\mathbf{u}_k\|^2_{\mathbf{R}_k} + \sum_{i=1}^{N_u} \frac{\tau_{ki}}{q_k}|u_{ki}|^{q_k}. \tag{23c}$$

In the previous set of equations $\|\mathbf{x}\|^2_{\mathbf{Q}} = \mathbf{x}^\mathsf{T}\mathbf{Q}^{-1}\mathbf{x}$ is the squared Mahalanobis distance, while $f(q_k|\mathbf{u}_k, \tau_{ki})$ is given by:

$$\begin{aligned} f(q_k|\mathbf{u}_k, \tau_{ki}) = N_u\ \log\Gamma(1/q_k) + \frac{1}{q_k}\sum_{i=1}^{N_u}(\tau_{ki}|u_{ki}|^{q_k} - \log\tau_{ki}) \\ + \frac{\beta_q}{q_k} + \left(\alpha_q + 1 - N_u\left(1 - \frac{1}{q_k}\right)\right)\log q_k, \end{aligned} \tag{24}$$

for $q_k \in [l_b, u_b]$.

It should be noted here that the solution of the optimization problem given by Eq. (23a) is calculated analytically in a straightforward manner, and that Eq. (23b) is solved efficiently using a brute force approach. As for the matrix $\mathbf{W}_k$, it is a by-product of the previous optimization process, since:

$$\mathbf{W}_k = \operatorname{diag}(w_{k1}, \ldots, w_{kn}, \ldots, w_{kN_u}) \text{ with } w_{kn} = \max\left(\epsilon, |\widehat{u}_{kn}|\right)^{\widehat{q}_k - 2}, \tag{25}$$

where ϵ is a small positive number avoiding infinite values and $\widehat{u}_{kn}$ is the n-th component of the optimal input vector $\widehat{\mathbf{u}}_k$.

Finally, to complete the estimation step of the proposed Bayesian filter (see step 3 of section 3), it remains to compute the Kalman gain $\mathbf{K}_k^{\mathbf{u}}$ and the predictive covariance matrix $\widetilde{\mathbf{P}}_k^{\mathbf{u}}$. By identification with Eq. (18), it comes:

$$\mathbf{K}_k^{\mathbf{u}} = (\mathbf{D}\mathbf{R}_k^{-1}\mathbf{D}^\mathsf{T} + \mathbf{T}_k\mathbf{W}_k)^{-1}\mathbf{D}^\mathsf{T}\mathbf{R}_k^{-1} \quad \text{and} \quad \widetilde{\mathbf{P}}_k^{\mathbf{u}} = (\mathbf{T}_k\mathbf{W}_k)^{-1}. \tag{26}$$

As a side note, since the optimization process is iterative, it is important to tell that it is initialized with the optimal shape parameter and input vector obtained at the previous time step, namely $\widehat{q}_{k-1}$ and $\widehat{\mathbf{u}}_{k-1}$. Note also that the solution of Eq. (23c) requires the implementation of another iterative process, whose solution at iteration j for a given set of parameters $(\widehat{\tau}_{ki}^{(j)}, \widehat{q}_k^{(j)})$ is given by :

$$\widehat{\mathbf{u}}_k^{(j)} = \mathbf{K}_k^{\mathbf{u}(j)}\, \mathbf{i}_k^{\mathbf{u}}, \tag{27}$$

where $\mathbf{K}_k^{\mathbf{u}(j)} = \left(\mathbf{D}\mathbf{R}_k^{-1}\mathbf{D}^{\mathsf{T}} + \mathbf{T}_k\mathbf{W}_k^{(j-1)}\right)^{-1}\mathbf{D}^{\mathsf{T}}\mathbf{R}_k^{-1}$ is the Kalman gain computed at the j-th iteration, while $\mathbf{W}_k^{(j)}$ is expressed as in Eq. (25).

4.4. Computational algorithms

The previously introduced sequential filters are developed through several algorithms. Alg. 1 is the computational version of the framework expressed in section 3 where the estimated input vector can be computed through the three different ways, for CDKF, SaBF and CBF. For CBF, Alg. 2 introduced an algorithmic view of the method to compute the targeted input vector $\widehat{\mathbf{u}}_k$ and the predictive covariance matrix $\widetilde{\mathbf{P}}_k^{\mathbf{u}}$.

The optimization method used for the calculation of the estimated input in SaBF is fully expressed in [21], hence the references in the algorithm below concern only CBF. However, the architecture of the optimization as well as the employed method are very similar. The tolerance set to stop the iterative algorithm is fixed at 10^{-3} for the experiments developed in the following sections. It corresponds to the value of the relative error δ between two successive iterations (see Alg. 2). Finally, it has been observed that

Algorithm 1: Generalized algorithm of Bayesian Filter

Input : $\mathbf{y}_k$, $\mathbf{A}$, $\mathbf{B}$, $\mathbf{C}$, $\mathbf{D}$, $\widehat{\mathbf{u}}_0$, $\mathbf{P}_0^{\mathbf{u}}$, $\widehat{\mathbf{x}}_0$, $\mathbf{P}_0^{\mathbf{x}}$, $\mathbf{Q}_k^{\mathbf{x}}$, $\mathbf{R}_k$, $\widehat{q}_0$

Output : $\widehat{\mathbf{u}}_k$, $\mathbf{P}_k^{\mathbf{u}}$, $\widehat{\mathbf{x}}_k$, $\mathbf{P}_k^{\mathbf{x}}$

0. Initialization

$$\widetilde{\mathbf{x}}_1 = \mathbf{A}\widehat{\mathbf{x}}_0 + \mathbf{B}\widehat{\mathbf{u}}_0 \text{ and } \widetilde{\mathbf{P}}_1^{\mathbf{x}} = \mathbf{A}\mathbf{P}_0^{\mathbf{x}}\mathbf{A}^{\mathsf{T}} + \mathbf{B}\mathbf{P}_0^{\mathbf{u}}\mathbf{B}^{\mathsf{T}} + \mathbf{Q}_0^{\mathbf{x}}$$

for each time step $k > 0$

1. Input estimation

$$\mathbf{i}_k = \mathbf{y}_k - \mathbf{C}\widetilde{\mathbf{x}}_k$$

(a) For CDKF:

$$\widetilde{\mathbf{P}}_k^{\mathbf{u}} = \mathbf{Q}_{k-1}^{\mathbf{u}} + \mathbf{P}_{k-1}^{\mathbf{u}}$$
$$\mathbf{K}_k^{\mathbf{u}} = \widetilde{\mathbf{P}}_k^{\mathbf{u}}\mathbf{D}^{\mathsf{T}}\left(\mathbf{D}\widetilde{\mathbf{P}}_k^{\mathbf{u}}\mathbf{D}^{\mathsf{T}} + \mathbf{R}_k\right)^{-1}$$
$$\widehat{\mathbf{u}}_k = \widetilde{\mathbf{u}}_k + \mathbf{K}_k^{\mathbf{u}}(\mathbf{i}_k - \mathbf{D}\widetilde{\mathbf{u}}_k)$$

(b) For SaBF and CBF:

$$\left(\widehat{\mathbf{u}}_k, \mathbf{K}_k^{\mathbf{u}}, \widetilde{\mathbf{P}}_k^{\mathbf{u}}, \widehat{q}_k\right) = \textbf{EstimationProcedure}$$
$$(\mathbf{D}, \mathbf{i}_k, \mathbf{R}_k, \widehat{\mathbf{u}}_{k-1}, \widehat{q}_{k-1})$$

$$\mathbf{P}_k^{\mathbf{u}} = \left(\mathbf{I} - \mathbf{K}_k^{\mathbf{u}}\mathbf{D}\right)\widetilde{\mathbf{P}}_k^{\mathbf{u}}\left(\mathbf{I} - \mathbf{K}_k^{\mathbf{u}}\mathbf{D}\right)^{\mathsf{T}} + \mathbf{K}_k^{\mathbf{u}}\left(\mathbf{C}\widetilde{\mathbf{P}}_k^{\mathbf{x}}\mathbf{C}^{\mathsf{T}} + \mathbf{R}_k\right)\mathbf{K}_k^{\mathbf{u}\mathsf{T}}$$

2. State estimation

$$\mathbf{K}_k^{\mathbf{x}} = \widetilde{\mathbf{P}}_k^{\mathbf{x}}\mathbf{C}^{\mathsf{T}}\left(\mathbf{C}\widetilde{\mathbf{P}}_k^{\mathbf{x}}\mathbf{C}^{\mathsf{T}} + \mathbf{R}_k\right)^{-1}$$
$$\widehat{\mathbf{x}}_k = \widetilde{\mathbf{x}}_k + \mathbf{K}_k^{\mathbf{x}}\left(\mathbf{i}_k - \mathbf{D}\widehat{\mathbf{u}}_k\right)$$
$$\mathbf{P}_k^{\mathbf{x}} = \left(\mathbf{I} - \mathbf{K}_k^{\mathbf{x}}\mathbf{C}\right)\widetilde{\mathbf{P}}_k^{\mathbf{x}}\left(\mathbf{I} - \mathbf{K}_k^{\mathbf{x}}\mathbf{C}\right)^{\mathsf{T}} + \mathbf{K}_k^{\mathbf{x}}\left(\mathbf{D}\mathbf{P}_k^{\mathbf{u}}\mathbf{D}^{\mathsf{T}} + \mathbf{R}_k\right)\mathbf{K}_k^{\mathbf{x}\mathsf{T}}$$
$$\mathbf{P}_k^{\mathbf{xu}} = -\mathbf{K}_k^{\mathbf{x}}\mathbf{D}\mathbf{P}_k^{\mathbf{u}}$$

3. State prediction

$$\widetilde{\mathbf{x}}_{k+1} = \mathbf{A}\widehat{\mathbf{x}}_k + \mathbf{B}\widehat{\mathbf{u}}_k$$
$$\widetilde{\mathbf{P}}_{k+1}^{\mathbf{x}} = \begin{bmatrix}\mathbf{A} & \mathbf{B}\end{bmatrix}\begin{bmatrix}\mathbf{P}_k^{\mathbf{x}} & \mathbf{P}_k^{\mathbf{xu}} \\ \mathbf{P}_k^{\mathbf{xu}\mathsf{T}} & \mathbf{P}_k^{\mathbf{u}}\end{bmatrix}\begin{bmatrix}\mathbf{A}^{\mathsf{T}} \\ \mathbf{B}^{\mathsf{T}}\end{bmatrix} + \mathbf{Q}_k^{\mathbf{x}}$$

end for

taking a lower value of the tolerance does not significantly affect the results of the estimation.

Algorithm 2: EstimationProcedure function for CBF

Input : $\mathbf{D}$, $\mathbf{i}_k$, $\mathbf{R}_k$, $\widehat{\mathbf{u}}_{k-1}$, $\widehat{q}_{k-1}$

Output : $\widehat{\mathbf{u}}_k$, $\mathbf{K}_k^{\mathbf{u}}$, $\widetilde{\mathbf{P}}_k^{\mathbf{u}}$, $\widehat{q}_k$

0. Initialization – $\widehat{q}_k^{(0)} = \widehat{q}_{k-1}$, $\widehat{\mathbf{u}}_k^{(0)} = \widehat{\mathbf{u}}_{k-1}$, $\delta = 1$

while $\delta > tol = 10^{-3}$

$j \leftarrow j + 1$

1. Compute $\widehat{\tau}_{ki}^{(j)}$ given $\widehat{\mathbf{u}}_k^{(j-1)}$ and $\widehat{q}_k^{(j-1)}$ from Eq. (23a).
2. Compute $\widehat{q}_k^{(j)}$ given $\widehat{\mathbf{u}}_k^{(j-1)}$ and $\widehat{\tau}_{ki}^{(j)}$ from Eqs. (23b).
3. Compute $\widehat{\mathbf{u}}_k^{(j)}$ and $\mathbf{W}_k^{(j)}$ given $\widehat{q}_k^{(i)}$ and $\widehat{\tau}_{ki}^{(j)}$ from Eqs. (23c) and (25).
4. Convergence monitoring: $\delta = \frac{\left\|\widehat{\mathbf{u}}_k^{(j)} - \widehat{\mathbf{u}}_k^{(j-1)}\right\|_2^2}{\left\|\widehat{\mathbf{u}}_k^{(ji-1)}\right\|_2^2}$

end while

$\widehat{\mathbf{u}}_k = \widehat{\mathbf{u}}_k^{(J)}$, $\widehat{q}_k = \widehat{q}_k^{(J)}$, $\widehat{\tau}_{ki} = \widehat{\tau}_{ki}^{(J)}$ and $\mathbf{W}_k = \mathbf{W}_k^{(J)}$

Compute $\mathbf{K}_k^{\mathbf{u}}$ and $\widetilde{\mathbf{P}}_k^{\mathbf{u}}$ from Eq. (26)

4.5. Discussion

The developed methods, particularly SaBF and CBF, offer several significant advantages in solving the effort estimation problem when the excitation field to be identified is spatially sparse. First, they operate online, which theoretically allows them to provide real-time estimates. In addition, they impose additional constraints on the solution (here the spartial sparsity of

the input vector), which allows to relax some conditions such as those related to the instantaneous inversion or the numerical stability [30], while providing high quality results. However, it is important to note that these advantages come with a higher algorithmic complexity, which may limit their practical use for real-time applications, where computational speed is essential. Therefore, their practical implementation needs to be carefully evaluated according to the specific time constraints of each application. As for CDKF, given the assumptions made, performances similar to AKF and DKF can be expected. Taking into account the correlation between state and input is an advantage for this method, but, as for AKF and DKF, it also requires the adjustment of the input covariance σ_u^2, which makes the method rather offline, since the optimization is performed over the entire reconstruction window [14, 20]. More generally, the proposed Bayesian formulation imposes the presence of a feedforward matrix $\mathbf{D}$, so at least one accelerometer must be used, while these methods require a measurement to be collocated with the excitation to achieve better performance (see sections 5.2 and 5.6). These requirements can be a disadvantage in certain practical situations where the installation of accelerometers is difficult or costly and the excitation region is inaccessible.

5. Numerical experiment

This section presents the application of the sequential filters developed above in a purely numerical context. Their performance is compared with each other, with special attention to the appearance of drift when only acceleration measurements are available. The focus of this application is on estimating the input vector, rather than the state vector, which may be

more relevant in some applications. Therefore, this problem is specifically dedicated to the force identification problem at sensor locations, rather than state reconstruction from the measurements.

5.1. Problem definition

The structure considered here is a stainless steel simply supported beam. The beam has a length of $L = 3$ m, with a cross-sectional area of $S = 1060$ mm^2 and a second moment of area of $I = 171$ mm^4. The material properties are $E = 210$ GPa for the Young's modulus and $\rho = 7850$ kg/m^3 for the density.

In the present numerical application, it is supposed that the beam undergoes a hammer impact at location $x_{\text{exc}} = 0.98$ m, measured from its left end. This type of excitation can be modeled by a Gamma-like function of shape parameter p and scale parameter θ [31], that is:

$$u_{\text{ref}}(t) = u_0 \left(\frac{t}{p\theta}\right)^p \exp\left(-\frac{t}{\theta} + p\right), \tag{28}$$

where u_0 is the force intensity. In this example, it is assumed that the structure is excited by a hammer equipped with a soft rubber tip, that excites only the low frequency modes of the beam. To reflect this assumption, the parameters of the input excitation are chosen such that $u_0 = 15$ N, $p = 8.7$ and $\theta = 0.6$ ms. In addition, a pre-trigger delay of 8 ms is applied at the beginning of the signal. This reference force is shown in Fig. 1a. Note that the applied hammer excitation has a cutoff frequency around 500 Hz, as shown in the Fig. 1b.

This excitation profile is used to generate the vibration response of the structure. Here, the acceleration data is measured by twenty sensors, dis-

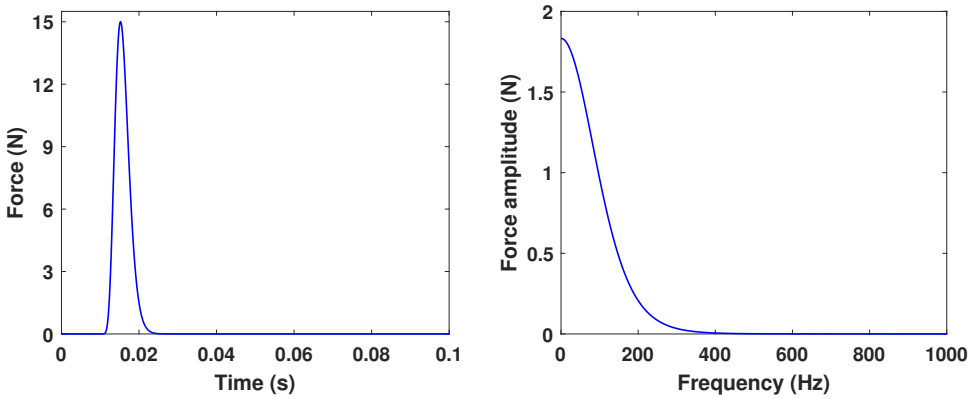

(a) (b)

Figure 1: Synthesized hammer impact excitation signal - (a) Time domain representation and (b) Frequency domain representation.

tributed along the beam as shown in Fig. 2. This distribution is intentionally not symmetric to avoid configurations where some information may be lost or redundant.

Figure 2: Location of the accelerometers and the impact location on the beam – (■) Hammer impact and (•) Accelerometers

A finite element model, consisting of 20 beam elements, is used to synthesize the measured data assuming a structural damping ratio of 0.01. The noiseless acceleration data are computed over 1 second using an unconditionally stable and second-order accurate Newmark's integration scheme with a time step size of 10 µs. The computed data is then corrupted by an additive

Gaussian white noise to simulate the measurement process, with a controlled signal-to-noise ratio (SNR) of 25 dB.

As for the discretized state-space representation, a zero-order hold discretization method combined with a modally reduced order model of the beam, containing all the vibration modes with a natural frequency below 1 kHz (i.e. 53 modes), is used to derive the system matrices $\mathbf{A}$, $\mathbf{B}$, $\mathbf{C}$ and $\mathbf{D}$ [14, 20, 32]. For the state-space model, a constant modal damping ratio is assumed and set to 0.01. It is also important to note at this stage that a collocated configuration is being considered, meaning that the inputs are identified at the sensor locations.

To properly implement the filters compared in this paper, it remains to define the initial conditions $(\widehat{\mathbf{x}}_0, \mathbf{P}_0^{\mathbf{x}})$ and $(\widehat{\mathbf{u}}_0, \mathbf{P}_0^{\mathbf{u}})$ as well as the covariance matrices $\mathbf{Q}_k^{\mathbf{x}}$ and $\mathbf{R}_k$. The initial state and input vectors $\widehat{\mathbf{x}}_0$ and $\widehat{\mathbf{u}}_0$ are zero vectors because the structure is initially at a rest and no force is applied on the structure before 8 ms. The corresponding covariance matrices $\mathbf{P}_0^{\mathbf{x}}$ and $\mathbf{P}_0^{\mathbf{u}}$ are assumed to be isotropic with a variance set to 10^{-20}, reflecting our confidence in knowing the initial conditions of the system. The noise covariance matrices $\mathbf{Q}_k^{\mathbf{x}}$ and $\mathbf{R}_k$ are also assumed to be isotropic and constant over time, with respective values of 10^{-20}, which was manually tuned and represents the high fidelity of the mechanical model, and 10^{-2}, which is the order of magnitude of the actual variance used to synthesize the noisy acceleration signals. Although the process noise and measurement noise variances have been set manually, it should be noted that their automatic estimation remains an active area of research [19, 33, 34]. That being said, for SaBF

and CBF, the initial shape parameter must also be specified. Here, $\widehat{q}_0$ is set to 1, because the spatial distribution of the input vector should be sparse, but it has been shown that this initial value has no real effect on the final result [21]. For AKF and CDKF, the covariance matrix associated with the fictitious equation on the input vector is assumed to be isotropic. Its variance, σ_u^2, is automatically adjusted using a specific criterion $J(\sigma_u^2)$. Here, σ_u^2 is sought so as to minimize the mean squared error of the obervations over the entire time window as in Refs. [20, 35]. For CDKF, this criterion is mathematically expressed as:

$$J(\sigma_u^2) = \frac{1}{n_t} \sum_{k=1}^{n_t} \|\mathbf{y}_k - \mathbf{C}\widehat{\mathbf{x}}_k - \mathbf{D}\widehat{\mathbf{u}}_k\|_2^2, \tag{29}$$

where n_t is the number of time steps.

Finally, three indicators are introduced to evaluate the quality of the estimated input vector. They provide an efficient way to measure the accuracy of the estimated vector compared to the actual excitation field.

First, the Global Relative Error (GRE) is an indicator that provides a measure of how close the estimated input vector is to the true input vector over the entire structure. The GRE equation is used to compare the estimated vector to the actual input values, providing a measure of the accuracy of the estimation:

$$\text{GRE} = \frac{\|\widehat{\mathbf{u}} - \mathbf{u}_{\text{ref}}\|_1}{\|\mathbf{u}_{\text{ref}}\|_1}. \tag{30}$$

$\mathbf{u}_{\text{ref}}$ and $\widehat{\mathbf{u}}$ represent respectively the reference and estimated input vectors defined over the entire estimation duration.

In addition to the Global Relative Error (GRE), two other indicators are proposed to locally measure the accuracy of the estimated input vector. The

Peak Error (PE) is a local indicator used to evaluate the accuracy of the estimated peak value. It compares the maximum intensity of the hammer impact estimated at the actual point force location $\widehat{u}^{\text{exc}}$ with that of the reference one $u_{\text{ref}}^{\text{exc}}$. This indicator is mathematically expressed as:

$$\text{PE} = \frac{\widehat{u}^{\text{exc}} - u_{\text{ref}}^{\text{exc}}}{u_{\text{ref}}^{\text{exc}}}. \tag{31}$$

The sign of PE indicates whether the estimated value is higher or lower than the target value.

The last indicator used to measure the accuracy of the estimated input vector is the Correlation Coefficient (CC). This indicator provides a measure of the overall accuracy of the estimated excitation history, $\widehat{\mathbf{u}}^{\text{exc}}$, when compared to the reference one, $\mathbf{u}_{\text{ref}}^{\text{exc}}$, at the actual impact point location. It is given by:

$$\text{CC} = \frac{\mathbf{u}_{\text{ref}}^{\text{exc}}\ \widehat{\mathbf{u}}^{\text{exc}^{\mathsf{T}}}}{\|\mathbf{u}_{\text{ref}}^{\text{exc}}\|_2\ \|\widehat{\mathbf{u}}^{\text{exc}}\|_2}. \tag{32}$$

5.2. Identification of the hammer impact

As a first application, the filters are compared with each other and with AKF [18] on the configuration described in the previous section. The estimation of the input time history presented in Fig. 3 shows that the peak value estimated by all the filters is close to the reference value of 15 N, although it is underestimated by about 50 mN for SaBF and CBF. On this figure, the AKF and CDKF are almost superimposed, as expected, since their hypotheses are somewhat similar. It is the same for SaBF and CBF, although CBF is slightly better than SaBF.

Furthermore, another very important aspect of the identification is the input behavior after the hammer impact has been identified: there is a residual value that causes the filter to diverge instead of remaining constant. This

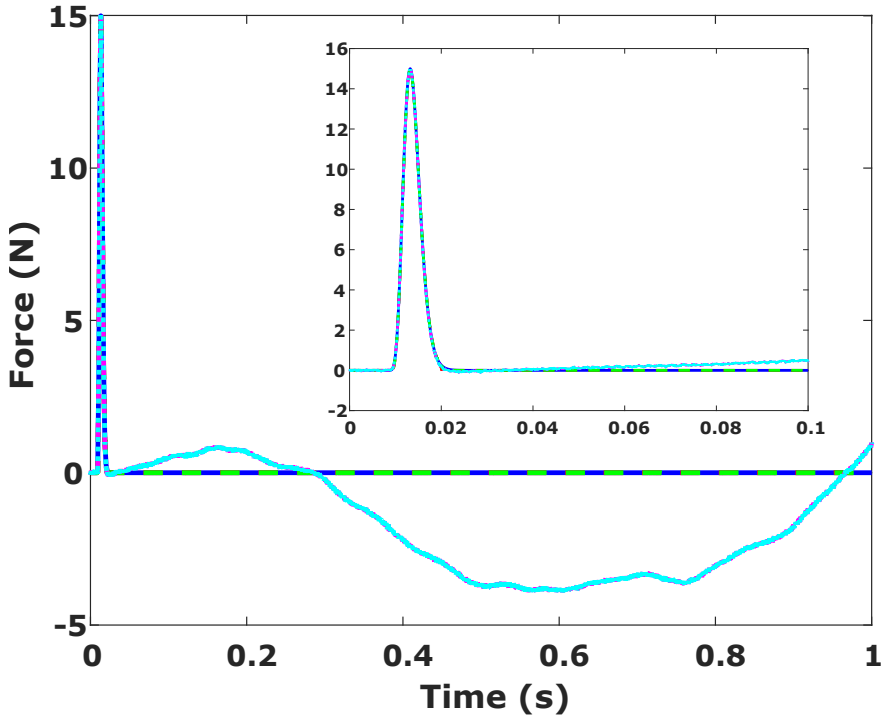

Figure 3: Time history of the estimated input for a duration of 1s and restricted to 0.1s for clarity - (—) Reference, (– –) SaBF, (– –) CBF, (– –) CDKF and (· · ·) AKF. SaBF and CDKF results are overlaid like those of AKF and CDKF.

phenomenon is called the drift effect, which characterizes the tendency of the identified variable to deviate from a constant value, in this case zero. This drift is clearly observed on AKF and CDKF immediately after the impact, when $t > 60$ ms. These two curves are quite superimposed, their respective maximum drift values are around 4 N after the impact, i.e. while $t > 20$ ms, at the excitation node. Their standard deviations are 1.70 N for both CDKF and AKF. On the contrary, no drift is observed for SaBF and CBF: the estimates stagnate after the actual shock, with a standard deviation that does not exceed 0.2 mN for SaBF and CBF.

Moreover, as shown in Fig. 3, both SaBF and CBF produce a more accurate identification of the impact than CDKF and AKF. Nevertheless, all filters identify the impact location well. Fig. 4 shows the estimated location and time history of the impact, according to each filter. As can be seen from the estimated input distributions of CDKF and AKF, the total duration of the estimation combined with the drift effect leads to a significant error in the estimated force: the drift effect 7.44 N over 1 s for both CDKF and AKF.

Furthermore, as shown in Table 1, the correlation between the results provided by SaBF and CBF and the actual force is very close to 100%, which is much higher than that of AKF and CDKF at about 33%. Meanwhile, the global error of the latter two is not in the same order of magnitude as the GRE of SaBF and CBF, at about 2%. The peak is always estimated with an error of about 0.5%.

Finally, the identification of impacts cannot be done online with CDKF

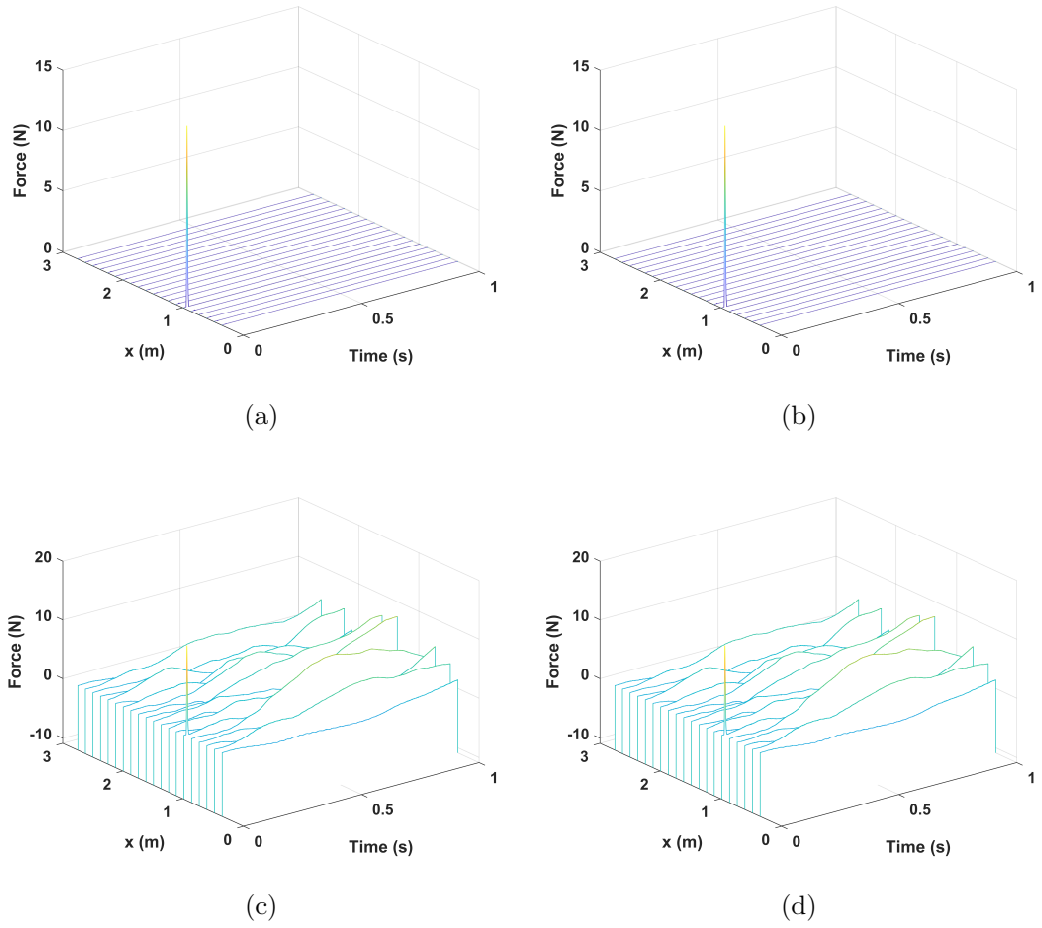

Figure 4: Estimated input distribution – (a) SaBF, (b) CBF, (c) CDKF and (d) AKF.

Table 1: Indicators value for each tested filter in the reference configuration over 1 s.

Filter	**GRE** (%)	**PE** (%)	**CC** (%)
SaBF	1.96	-0.38	99.99
CBF	1.51	-0.35	99.99
CDKF	517.37	0.07	33.07
AKF	517.38	0.07	33.10

and AKF, since they require a proper tuning of the covariance matrix $\mathbf{Q}_k^{\mathbf{u}}$. The functional $J(\sigma_u^2)$ used to select the variance parameter σ_u^2 for AKF and CDKF is shown in Fig. 5 for information. It can be observed that the functional has the same form for AKF and CDKF. Although the optimal values differ by several orders of magnitude, it can be observed, as in Ref [36], that the value of the functional is relatively flat from $\sigma_u^2 \approx 10^{10}$, meaning that in this case σ_u^2 can take any value between 10^{10} and 10^{40} without affecting the estimation of the mean state and input vectors. In particular, σ_u^2 could be chosen as the corner of the L-shaped curves. In addition, even if a shock is initially identified in terms of its intensity and location, in the long run, the input estimate may change in the instant immediately following, potentially leading to misunderstandings about the actual phenomenon that is occurring.

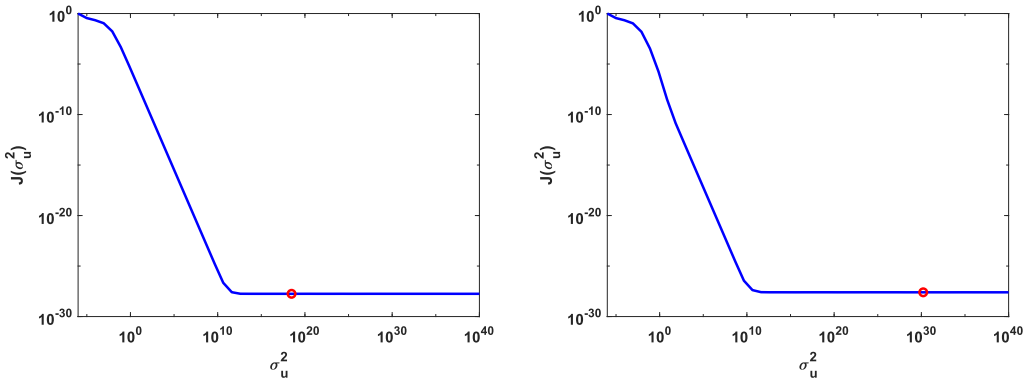

(a) (b)

Figure 5: Plot of the functional to be minimized for (a) AKF and (b) CDKF – (—) $J(\sigma_u^2)$ and (○) minimum of the functional ($\sigma_u^2 = 3\times10^{18}$ for AKF and $\sigma_u^2 = 1.5\times10^{30}$ for CDKF).

5.3. Influence of the measurement noise

In engineering practice, certain parameters can significantly influence the quality of the estimated solutions. One such parameter is the measurement noise level, which is of particular interest. Therefore, the aim of this section is to evaluate the influence of this parameter on the performance of the filters discussed in this paper.

The noise added to the acceleration data is artificially increased to the point where the SNR has dropped from 25 dB to 15 dB. This change is reflected in the results, especially in the time history. As shown in Fig. 6, both AKF and CDKF drift up after the impact (almost superimposed), while the time histories of the SaBF and CBF remain almost constant around 0 N with a standard deviation around 2.7 mN and 6.9 mN, respectively, while it spikes up to around 5.43 N for AKF and CDKF. As in the initial configuration, the estimates using AKF and CDKF, as well as SaBF and CBF, are superimposed.

Comparing the results of AKF and CDKF with those previously obtained with a higher SNR, it can be concluded that the higher the noise, the steeper the slope of this drift, and thus, the influence of the drift along the total duration increases. The maximum estimated values are slightly lower than the expected value of 15 N, around 0.18 N. Furthermore, although the impact is correctly located on Fig. 7, the drift reappears at almost all the identification points, with its own deviations and slopes. For the sake of clarity, all the figures presented in the rest of this section will only show the results of the

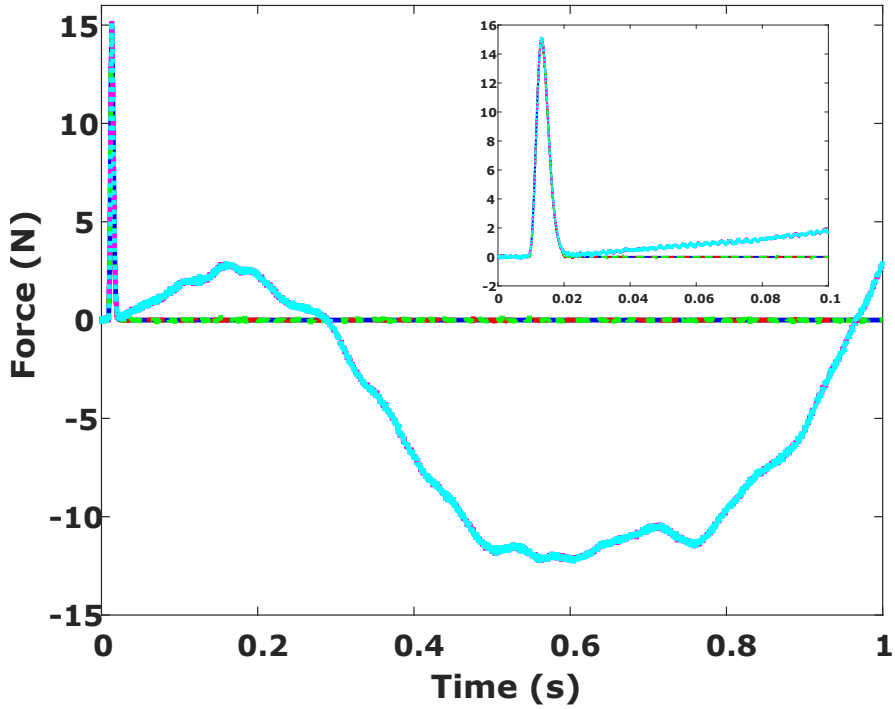

Figure 6: Time history of the estimated input with a SNR of 15 dB for a duration of 1s and restricted to 0.1 s for clarity - (—) Reference, (– –) SaBF, (– –) CBF, (– –) CDKF and (· · ·) AKF. SaBF and CDKF results are overlaid like those of AKF and CDKF.

filters on a duration of 0.3 s. However, the indicators remain computed over the whole duration, here 1 s.

Since SaBF and CBF eliminate the drift, the global error in the identification of the mechanical excitation is approximately reduced compared to that of AKF or CDKF. The maximum absolute value of the drift reaches about 34 N for CDKF and AKF at the end of the numerical experiment, when $t = 1$ s.

This large error, due to the high level of noise in the data, is unacceptable to answer the force identification problem. Therefore, the development of strategies such as SaBF and CBF, which are based on new hypotheses during the prediction step, makes a lot of sense, as they provide accurate results in terms of time history and location of the impact, while not drifting up (or down).

As expected, all the indicators in Table 2 are favorable to SaBF and CBF, their correlation coefficients remain close to 100% while it drops to 11% for CDKF and AKF. This can also be observed on the GRE indicator, since tha values obtained for AKF and CDKF dramatically increase due to the high influence of the drift.

5.4. Influence of the number of sensors

The number of sensors determines the amount of data available for the input-state estimation process. As the number of sensors increases, the computation time increases due to the larger amount of information to process. However, a larger number of sensors does not obviously lead to a better reconstruction of the impact, as the problem is mathematically ill-posed. Here

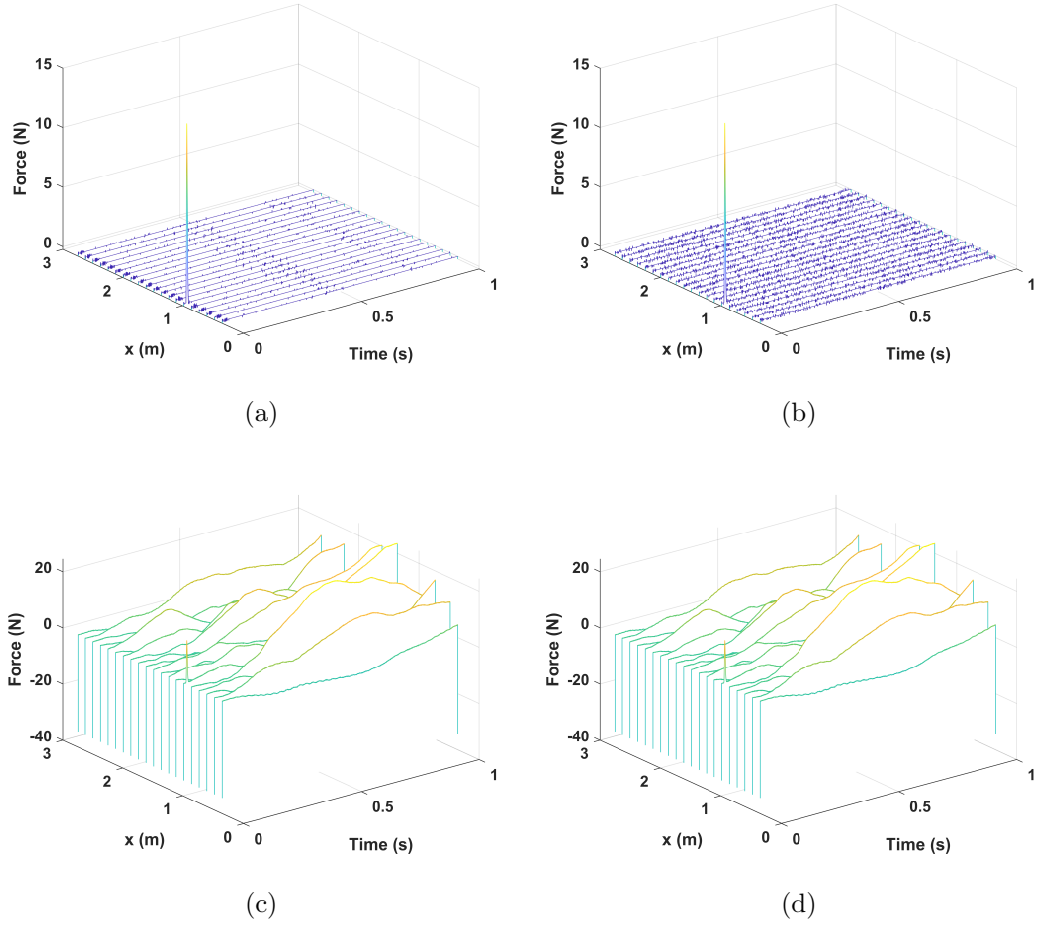

Figure 7: Estimated input distribution for a SNR of 15 dB – (a) SaBF, (b) CBF, (c) CDKF and (d) AKF.

Table 2: Indicators values for each tested filter for a SNR of 15 dB.

Filter	**GRE** (%)	**PE** (%)	**CC** (%)
SaBF	8.62	-0.28	99.99
CBF	6.05	0.06	99.99
CDKF	1636	1.23	11.14
AKF	1636	1.23	11.15

after, the number of sensors is reduced to four, distributed along the structure. The following Fig. 8 shows the estimated input at the impact node. The maximum identified value is close to the real impacting one of 15 N, with an error less than 64 mN for each filter.

As shown in Fig. 9, the impact is well located and its time history is very similar to the reference one. The reduction in the number of sensors does not significantly affect the quality of the estimation for SaBF and CBF, although the standard deviation is slightly better than that found with the 20-sensor configuration at 0.8 mN for both filters. However, it has a significant positive effect on AKF and CDKF, as the standard deviation is now found to be around 0.1 N and the drift almost disappears over the whole 1 s duration.

Finally, Table 3 summarizes all the indicators used to objectively compare the four filters. Once again, both SaBF and CBF provide better results than AKF and CDKF, with the lowest Global Relative Error and the highest Correlation Coefficient. However, it is worth noting that the indicators values for AKF and CDKF improve significantly when the number of sensors is limited.

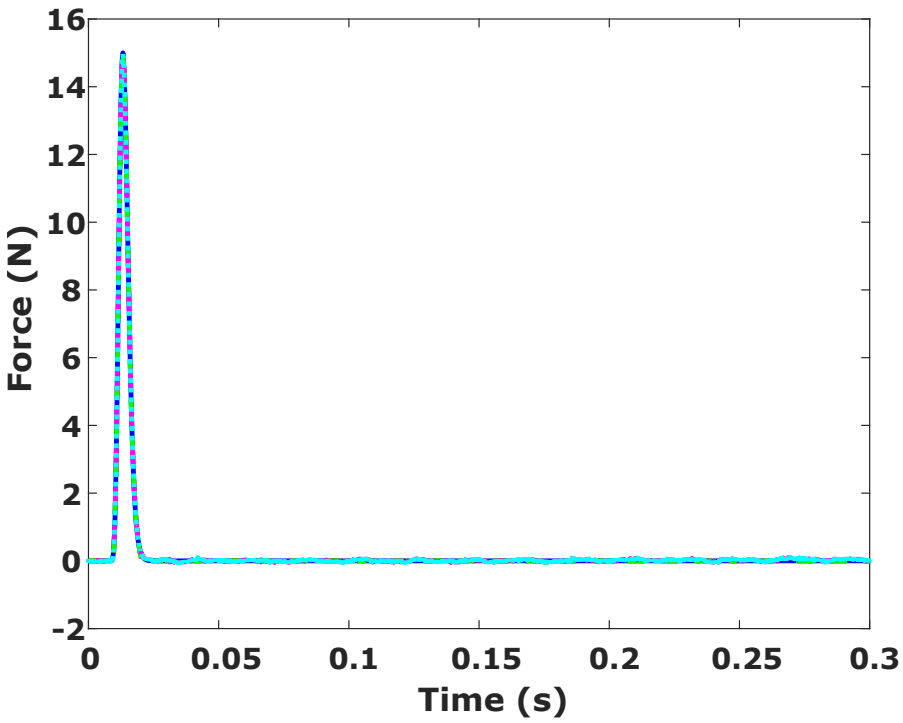

Figure 8: Time history of the estimated input with six sensors mounted on the structure - (—) Reference, (– –) SaBF, (– –) CBF, (– –) CDKF and (· · ·) AKF. All the curves are almost superimposed.

Table 3: Indicators values for each tested filter for a set of four sensors over 1 s.

Filter	**GRE** (%)	**PE** (%)	**CC** (%)
SaBF	1.35	-0.43	99.99
CBF	1.33	-0.42	99.99
CDKF	6.21	-0.27	98.82
AKF	6.21	-0.27	98.81

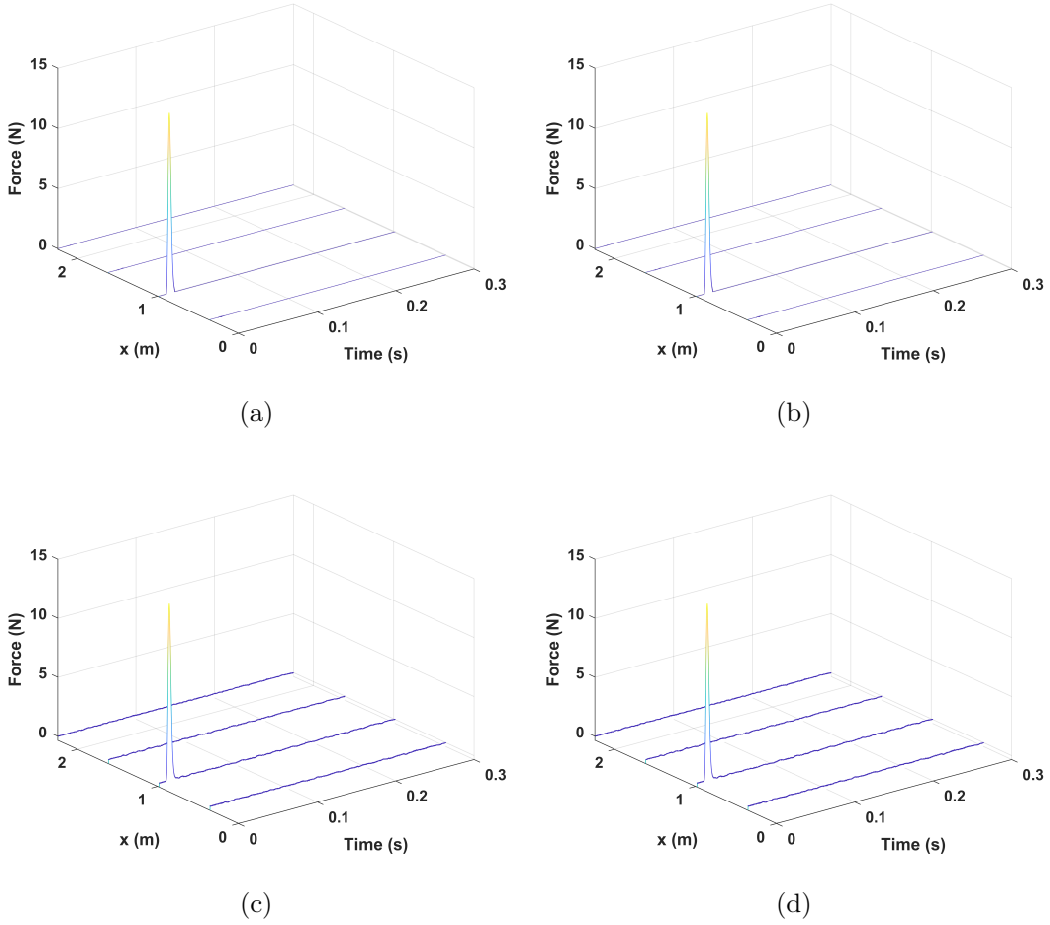

(a) (b)

(c) (d)

Figure 9: Estimated input distribution for a set of four sensors – (a) SaBF, (b) CBF, (c) CDKF and (d) AKF.

5.5. Case of a non-transient excitation

To complete the numerical experiment, a sinusoidal signal is added at the measurement point $x_s = 1.74$ m, so that the configuration remains collocated. The continuous excitation is a four-period sine wave, with an amplitude of 15 N, the same as the hammer impact, and a frequency of 20 Hz and starting at 5 ms. As shown in Figs. 10 and 11, both the hammer impact and the sinusoidal oscillation are correctly estimated for the sparse filters, both in terms of location and time history. Their respective standard deviations at the non-excited points are still around 60 mN for SaBF and 42 mN for CBF. However, this is not the case for both AKF and CDKF, for which the drift appears immediately after the end of the excitation signals. Finally, the analysis of the indicators collected in Table 4 confirms the results obtained in the previous sections, since CBF performs slightly better than SaBF, while AKF and CDKF give identical results.

Table 4: Indicators values for each tested filter in case of multiple excitation signals over 1 s.

Filter	**GRE** (%)	**CC** (hammer - %)	**CC** (Sine - %)
SaBF	5.36	99.96	99.99
CBF	3.79	99.98	99.99
CDKF	944.83	10.37	47.29
AKF	944.84	10.37	47.29

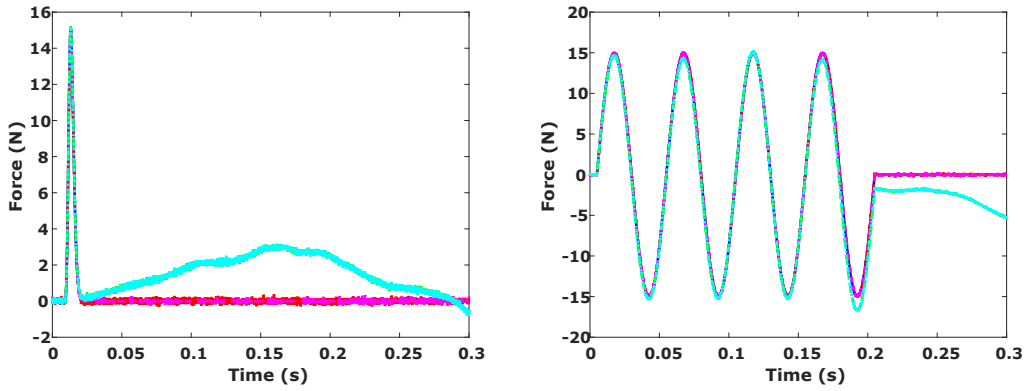

(a) (b)

Figure 10: Time history of the estimated (a) hammer excitation and (b) the sine wave excitation - (—) Reference, (– –) SaBF, (– –) CBF, (– –) CDKF and (· · ·) AKF. SaBF and CDKF results are overlaid like those of AKF and CDKF.

5.6. Case of a non-collocated configuration

A non-collocated configuration is created by moving the accelerometers by of a few centimeters to the left. The spacing is set to 3.2 cm, which is a quarter of the distance between two sensors. The results obtained by SaBF, CBF and CDKF are shown in Figs. 12 and 13. In fact, the automatic selection procedure of the input variance parameter σ_u^2 (see Eq. (29)) does not allow to obtain convergent results for AKF, as shown in Table 5.

In the case of a small gap with the actual impact location, it does not induce any large differences with the collocated configuration, since the estimation remains consistent with the results exposed in the sections above. The impact is actually well located and its intensity is well identified, the standard variations after impact have not been affected as they remain below 0.3 mN for both SaBF and CBF. Finally, Table 5 shows that here again

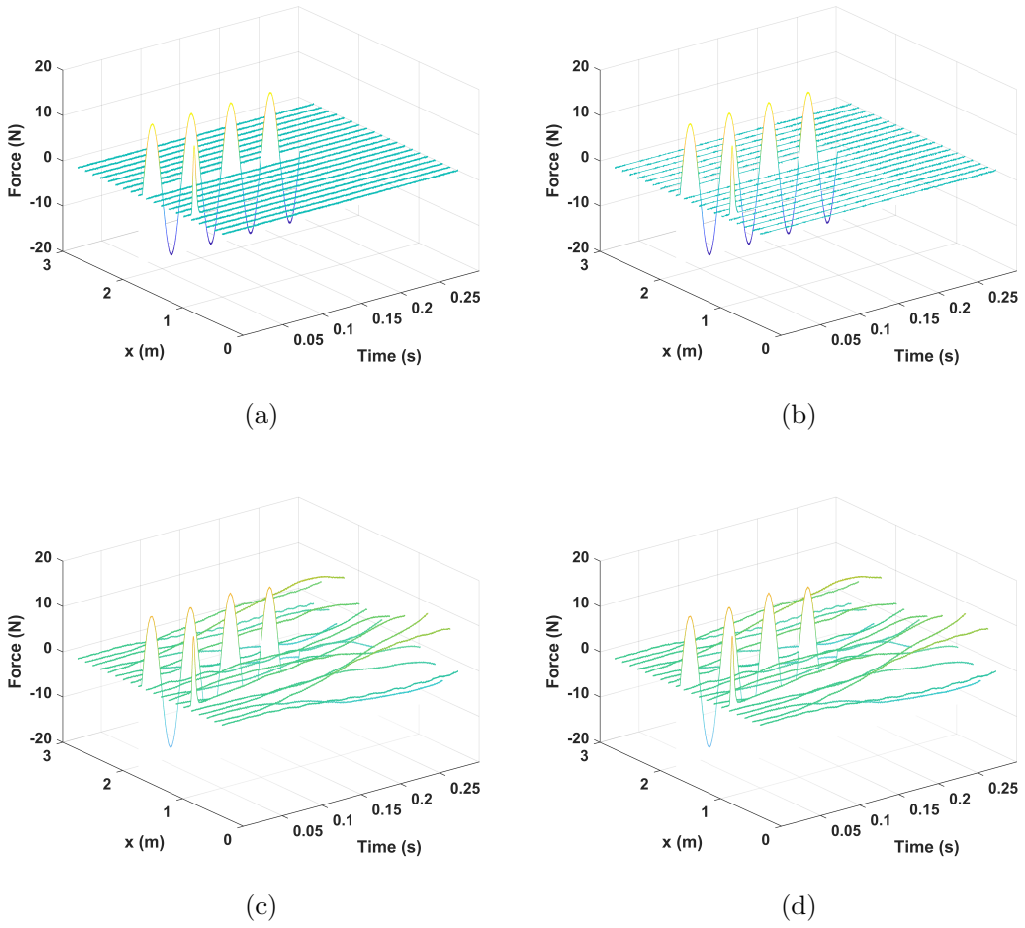

Figure 11: Spatial distribution of the estimated impact of the hammer and the estimated oscillating signal with the same intensity of 15 N – (a) SaBF, (b) CBF, (c) CDKF and (d) AKF.

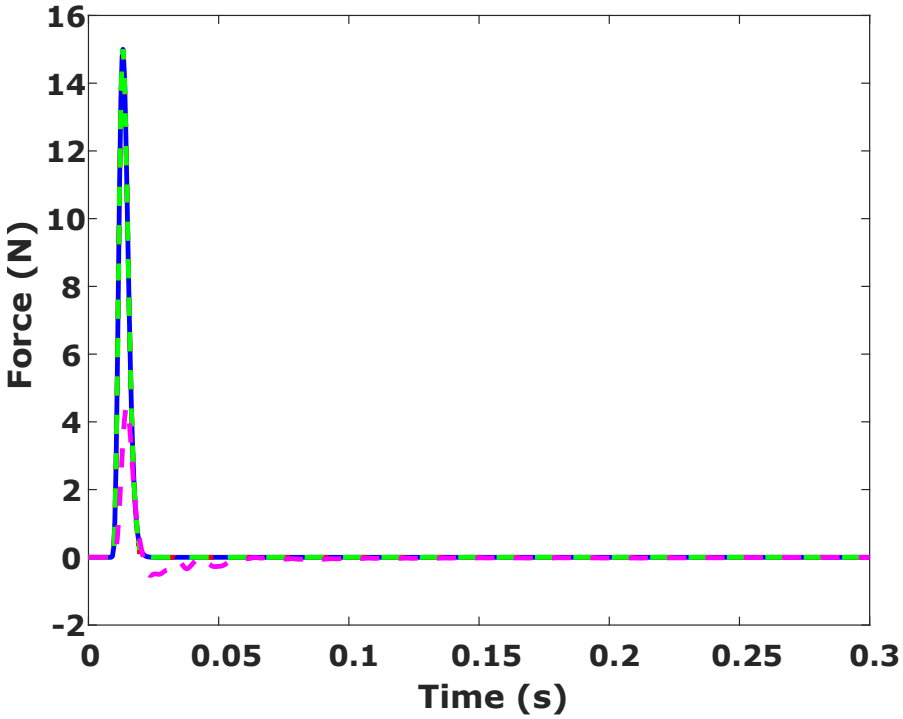

Figure 12: Time history of the estimated input in a non-collocated configuration - (—) Reference, (– –) SaBF, (– –) CBF, (– –) CDKF and (· · ·) AKF. SaBF and CDKF results are overlaid.

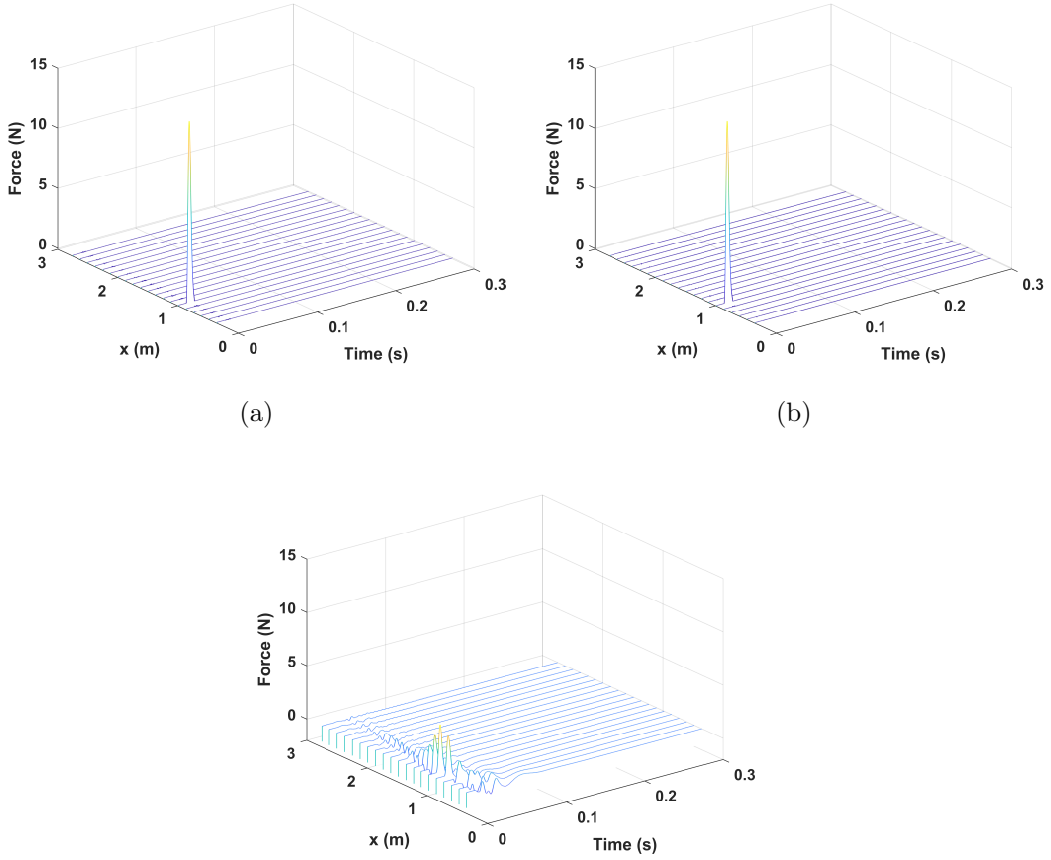

(a)

(b)

(c)

Figure 13: Spatial distribution of the estimated impact of the hammer in a non-collocated configuration – (a) SaBF, (b) CBF and (c) CDKF

CBF performs slightly better than SaBF. For CDKF, the estimated excitation field is oversmoothed, which explains the poor values of the GRE and PE indicators. However, no drift is observed, as shown by the value of the CC indicator.

Table 5: Indicators values for each tested filter in a non-collocated configuration over 1 s.

Filter	**GRE** (%)	**PE** (%)	**CC** (%)
SaBF	2.35	-0.06	99.99
CBF	1.61	-0.02	99.99
CDKF	108.80	-70.48	86.69
AKF	8.5×10^{6}	9.08×10^{5}	2.8×10^{-3}

As already reported in the literature, it has been observed that if the distance between the measurement point and the actual impact is too large (typically half of the distance between two sensors), the estimation becomes erroneous, because the ill-conditioning of the problem increases [14].

5.7. State reconstruction

State estimation can be of primary interest in some applications, so this section will shed some light on the performance of the considered filters for estimating the system state variables, although this is not the main purpose of the paper.

The time history of the displacement and velocity at $x = 1.74$ m is shown in Fig. 14. From a qualitative point of view, all the filters identify the system state very accurately. This local observation is globally confirmed by the analysis of the GRE indicator, summarized in Table 6, which shows that

SaBF and CBF perform slightly better than CDKF and AKF. The latter information is interesting to note because the estimate of the input vector obtained from AKF and CDKF experience a large drift (see section 5.2).

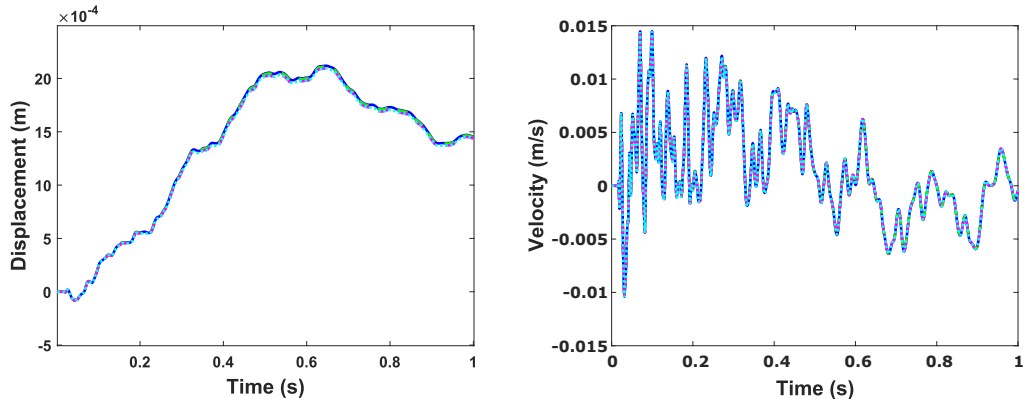

(a) (b)

Figure 14: Reconstruction of the state variables at $x = 1.74$ m for each filter: (a) Displacement and (b) Velocity - (—) Reference, (– –) SaBF, (– –) CBF, (– –) CDKF and (· · ·) AKF. SaBF and CDKF results are overlaid like those of AKF an CDKF.

6. Real-world application

The purpose of this section is to confirm the results of the numerical experiment in a real environment. The objective of this experiment is to evaluate the performance of the proposed filters in real operating conditions. This will help to determine the validity and usefulness of the filter through a real force identification case of a hammer impact.

Table 6: GRE values of the state variables for each tested filter in the reference configuration.

Filter	**GRE** (Displacement - %)	**GRE** (Velocity - %)
SaBF	0.46	0.86
CBF	0.36	0.67
CDKF	3.01	1.32
AKF	3.01	1.32

6.1. Description of the experimental set-up

The structure is a thin aluminum plate mounted on a dedicated support that reproduces the simply supported boundary conditions as accurately as possible. The plate is 420 mm long, 360 mm wide and 3 mm thick. The edges of the plate are glued to thin blades that are clamped in a rigid frame. These blades must have the right balance between flexibility and stiffness: they must be able to satisfy the degrees of freedom of rotation while supporting the weight of the plate and restraining the translation of the plate.

In this experiment, five 352C22 PCB Piezotronics sensors are mounted on the plate: 4 are located at points that are neither vibration nodes nor anti-nodes as much as possible, the last is collocated with the excitation in order to satisfy the instantaneous inversion constraint [30]. The excitation is generated by an impact hammer equipped with a load cell and connected to a vibration analyzer. A rubber tip is used to excite all the low frequency modes of the structure, i.e. below 2 kHz. The positions of the sensors as well as the impacted node are shown in Fig. 15, the real experimental setup is also provided next to the schematic representation for a better understanding.

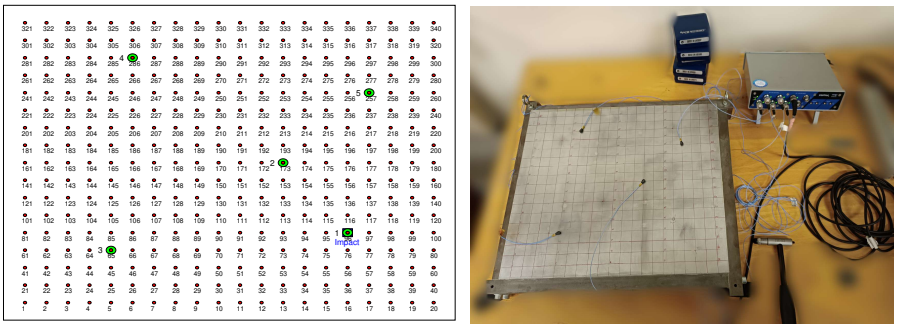

(a) (b)

Figure 15: Location of the accelerometers and the hammer impact on the grid used to perform the EMA – – (•) EMA grid, (■) Hammer impact and (•) Accelerometers

Fig. 16 is composed of the time history of the hammer impact and its frequency domain representation. Its maximum value is 27.78 N and it was recorded for a duration of 1 s, with a sampling frequency of 8192 Hz. This figure shows in particular that most of the impact energy is concentrated below 2 kHz. In this respect, and following the recommendations of Lourens et al. [14], the acquired vibration data are filtered at 2 kHz (eigenfrequency of the last mode considered in the modal analysis) with an eighth-order Chebyshev type I and resampled at twice this value with the nearest power of 2, i.e. 4096 Hz. These filtering and resampling steps are used to attenuate the influence of the out-of-band modes that are actually present but not considered in the model. In other words, this signal processing allows to reduce the size of the modal model used to define the state-space matrices $\mathbf{A}$, $\mathbf{B}$, $\mathbf{C}$ and $\mathbf{D}$ of the system.

The modal model of the structure is derived from an Experimental Modal Analysis (EMA). Frequency Response Functions (FRF) are recorded for the

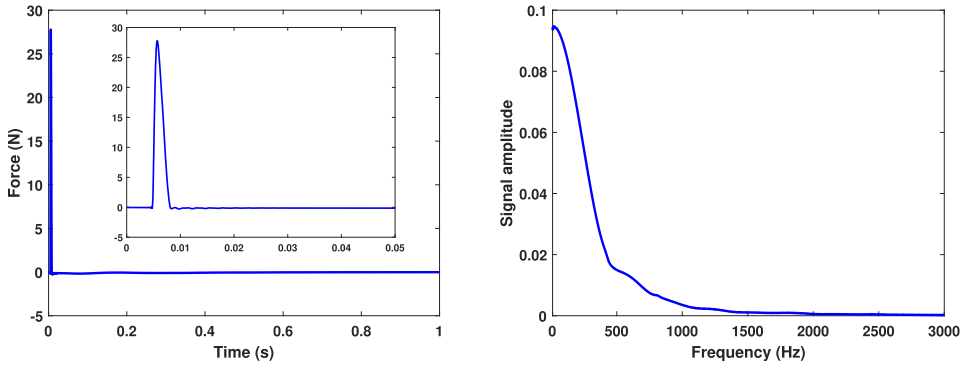

(a) (b)

Figure 16: Hammer impact measured at node 96 – (a) Time history and (b) Frequency spectrum

set of available sensors and the first vibration modes of the plate are extracted. The frequencies of the eigenmodes as well as the modal damping factors are thus obtained and reported in Table 7. The theoretical values are also included in for comparison. The small existing gap can be explained by the difference between the model used to compute these eigenmodes (geometry, boundary conditions, ...) and the real experimental setup. Considering the cut-off frequency of the excitation (see Fig. 16), only the first 23 modes are considered as interesting for the reconstruction.

Finally, as for the integration scheme used to derive the discretized state-space model, the explicit generalized-α scheme was chosen to compute the modally reduced state-space matrices of the plate, because of its second-order accuracy property [31].

Table 7: Table of the frequencies and damping coefficients for the vibration modes retained in the modal basis.

Mode ID	**Theoretical eigenfrequency (Hz)**	**Experimental eigenfrequency (Hz)**	**Experimental damping factor (%)**
1	98,2	106,2	7,85
2	222,9	226,7	0,26
3	267,9	271,7	0,59
4	392,6	392,1	0,17
5	430,7	432,2	0,11
6	550,8	547,8	0,13
7	600,5	598,0	0,24
8	675,5	670,3	0,08
9	721,7	719,8	0,08
10	883,4	872,2	0,27
11	891,4	890,3	0,18
12	946,9	934,5	0,18
13	1071,6	1061,4	0,07
14	1095,8	1090,8	0,08
15	1174,3	1159,1	0,07
16	1265,6	1253,7	0,07
17	1456,1	1448,2	0,30
18	1553,1	1539,5	0,06
19	1580,8	1559,0	0,09
20	1722,8	1699,3	0,08
21	1788,7	1761,5	0,07
22	1944,5	1913,9	0,09
23	2005,7	1971,9	0,07

6.2. Reconstruction of the hammer impact

As in section 5, a comparison is made between the sequential filters proposed in this paper and the mainstream filter existing in the literature, namely AKF. The results of SaBF, CBF and CDKF are again superimposed on those of AKF to evaluate their performance.

In order to use the filters properly, the initial state and input conditions must be defined, as well as the covariance matrices associated with the process and measurement noises. The initial state and input vectors $\widehat{\mathbf{x}}_0$ and $\widehat{\mathbf{u}}_0$ are zero vectors because the structure is initially at a rest and no force is applied to the structure before 5 ms. The corresponding covariance matrices $\mathbf{P}_0^{\mathbf{x}}$ and $\mathbf{P}_0^{\mathbf{u}}$ are assumed to be isotropic with a variance set to 10^{-20}, reflecting our confidence in knowing the initial conditions of the system. The noise covariance matrices $\mathbf{Q}_k^{\mathbf{x}}$ and $\mathbf{R}_k$ are also assumed to be isotropic and constant over time, with respective values of 10^{-20}, due to the signal processing implemented to build an accurate state-space model, and 10^{-1}, which has been estimated from the post-processed acceleration signals. For SaBF and CBF, the initial shape parameter must also be specified. Here, $\widehat{q}_0$ is set to 1, because the spatial distribution of the input vector should be sparse. For AKF and CDKF, the covariance matrix associated with the fictitious equation on the input vector is assumed to be isotropic. As in the numerical experiment, its variance is automatically adjusted by minimizing the MSE of the observations over the whole time window.

The location of the impact as well as the time history are estimated thanks to the measurements of the five sensors over a time window of 1 s. This

window can be reduced to 0.05 s for clarity, which is a sufficient duration to represent the estimation of the time history. As shown in Fig. 17, the solutions provided by SaBF and CBF outperform the other estimates, as expected after the numerical experiments. The maximum intensity of the peak is well identified by all the different filters, with an absolute error lower than 0.1 N. However, the behavior thereafter, which is still not acceptable for CDKF and AKF: the drift effect appears with almost the same slope for both filters. SaBF and CBF remain close to the value after the shock at $t > 10$ ms, with a standard deviation of about 0.2 N. This is due to the sparsity constraint imposed on the input vector during the filtering process.

As for the estimated excited node, all filters provide an accurate estimate of the location of the impact. In terms of force intensity, the time history of the force actually experienced by node 96 is shown in Fig. 18 for the entire structure. For SaBF and CBF, the drift effect is canceled at each identification point, with a total standard deviation of 0.1 N. The drift appears in the results of AKF and CDKF, with the highest slope at the impacted node. The drift increases to 4.53 N for CDKF and 6.01 N for AKF after only 0.05 s.

To fully compare the filters, the indicators developed in section 5.1 are also used in this experimental case. It can be seen that SaBF and CBF produce a more accurate identification in almost all categories presented in Table 8, as expected after the numerical experiment. With a better Global Relative Error and therefore a better Correlation Coefficient, SaBF and CBF identify the impact more accurately. Note that the GRE and CC values can't be compared with those from the numerical study because the total time is

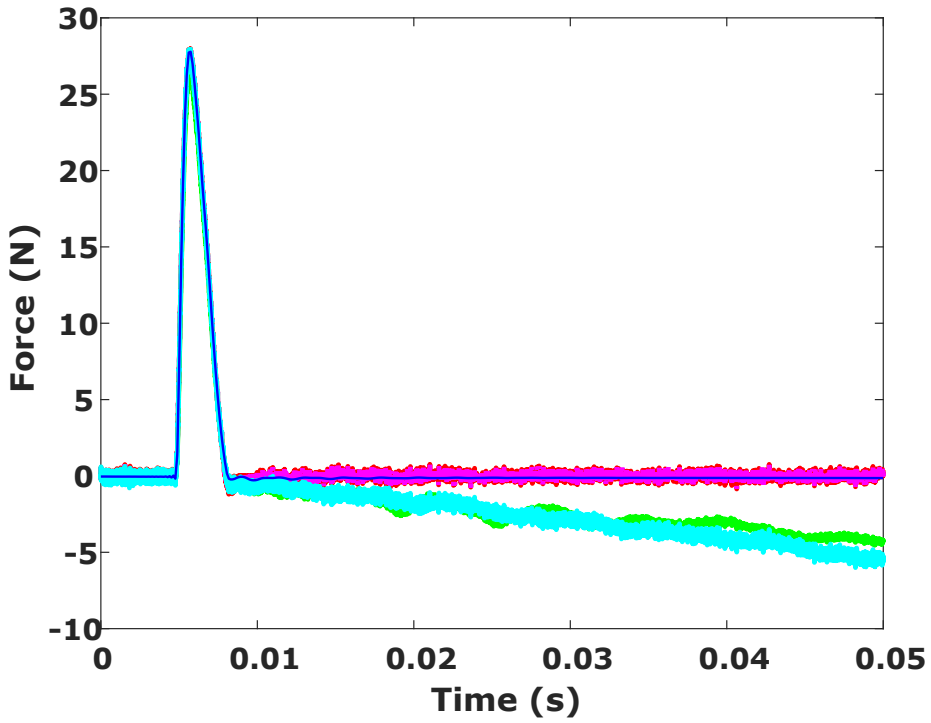

Figure 17: Time history of the estimated impact of the hammer locally on node 96 - (—) Reference, (– –) SaBF, (· · ·) CBF, (– · –) CDKF and (– –) AKF. SaBF and CDKF results are overlaid like those of AKF an CDKF.

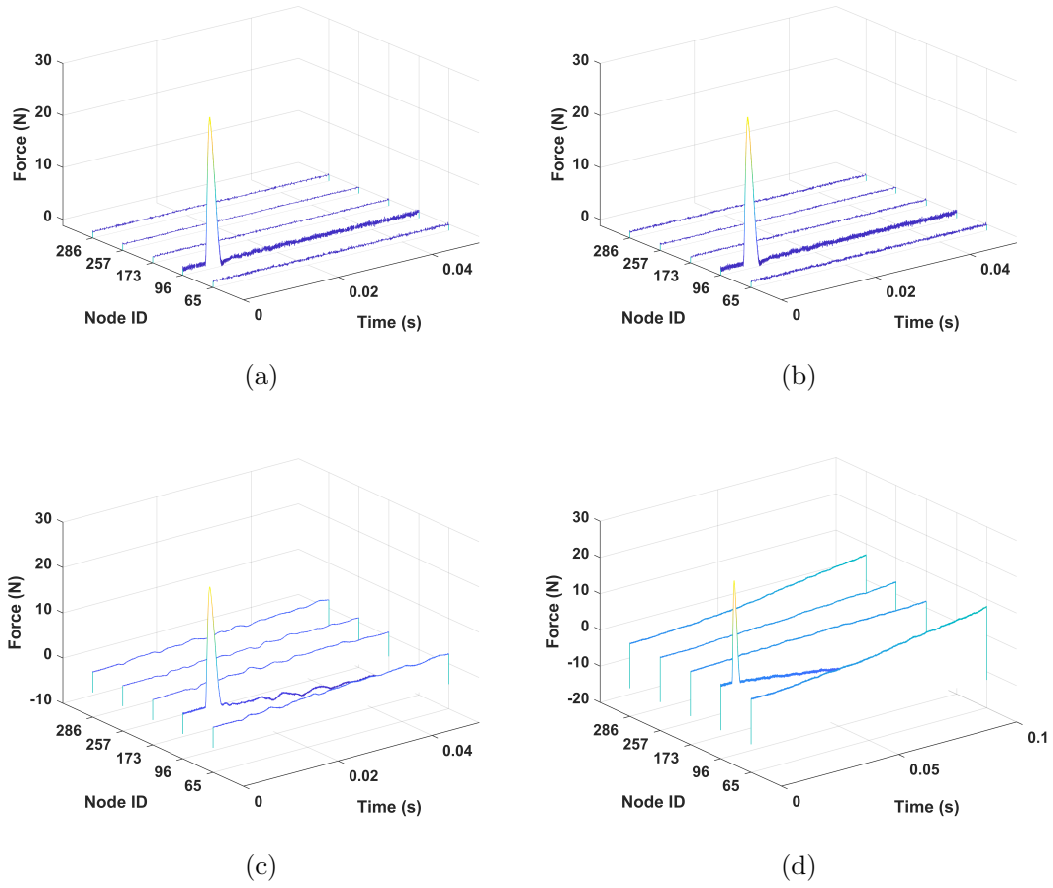

Figure 18: Spatial distribution of the estimated impact of the hammer for an estimated SNR of 22dB – (a) SaBF, (b) CBF, (c) CDKF and (d) AKF.

not the same, so the influence of the drift on both these two indicators is relatively small. CDKF gives slightly worse results than the AKF in this particular scenario : the error on the maximum intensity of the peak (PE) is the worst, and it has quadrupled with respect to the numerical study, while the PE of the other filters has remained constant (below 1%). Finally, the Correlation Coefficient of these two filters are almost equivalent.

Table 8: Indicators values for each tested filter for the considered experiment.

Filter	**GRE** (%)	**PE** (%)	**CC** (%)
SaBF	4.76	-0.79	99.88
CBF	4.53	-0.72	99.87
CDKF	37.82	-4.61	86.80
AKF	55.41	0.66	84.35

7. Conclusion

This paper presents two novel sequential Bayesian filters, the Correlated Dual Kalman Filter (CDKF) and the Component Bayesian Filter (CBF), for solving the input-state estimation problem. The goal of this work is to incorporate prior knowledge about the spatial distribution of the sources that excite a structure, while maintaining a sequential approach. To achieve this, we used a general Bayesian formulation of the problem, and extended it by introducing new hypotheses to develop the proposed filters.

CDKF is based on a generalization and a correction of two sequential filters developed in the literature, namely the Sequential Bayesian Filter and the

Dual Kalman Filter. As shown in this paper, it provides quite accurate results, barely better than those of AKF, which is certainly one of the most cited filters in the literature. This can be explained by the fact that the probability distribution maintains a non-zero mean and the correlation between the state and input vectors during the filtering process. Nevertheless, this original filter is still affected by the drift effect. To mitigate this problem, an improvement of the Sparse Adaptive Bayesian Filter (SaBF) presented in a previous work has been proposed through its component version (CBF). These approaches involve multiple parameters that are optimally estimated using a nested Bayesian optimization procedure. The results show that CBF is slightly more accurate than SaBF for force identification, and it outperforms AKF as well as CDKF. However, its computational cost is higher due to the optimization of a larger number of parameters. An interesting side effect of this sparsity adaption property is that it helps to avoid drift when only acceleration measurements are used.

Overall, the results presented in this paper demonstrate the effectiveness of the proposed filters in identifying spatially sparse excitation sources. The incorporation of prior knowledge about the spatial distribution of the sources that excite a structure results in more accurate and efficient filters.

References

[1] H. R. Busby and D. M. Trujillo. Solution of an inverse dynamics problem using an eigenvalue reduction technique. *Computers & Structures*, 25 (1):109–117, 1987.

[2] L. J. L. Nordström. A dynamic programming algorithm for input esti-

mation on linear time-variant systems. *Computers Methods in Applied Mechanics and Engineering*, 195:6407–6427, 2006.

[3] R. T. Jones, J. S. Sirkis, and E. J. Friebele. Detection of impact location and magnitude for isotropic plates using neural networks. *Journal of Intelligent Material Systems and Structures*, 8:90–99, 1997.

[4] K. Worden and W. J. Staszewski. Impact location and quantification on a composite panel using neural networks and a genetic algorithm. *Strain*, 36 (2):61–68, 2000.

[5] J. M. Zhou, L. Dong, W. Guan, and J. Yan. Impact load identification of nonlinear structures using deep recurrent neural network. *Mechanical Systems and Signal Processing*, 133:106292, 2019.

[6] P. O'Donoghue, O. Robin, and A. Berry. Time-resolved identification of mechanical loadings on plates using the virtual field method and deflectometry measurement. *Strain*, 54:e12258, 2018.

[7] N. Aujogue and A. Ross. Transient force analysis technique to identify time-varying loads and defects on plates. In *Proceedings of the 26th International Congress on Sound and Vibration*, Montréal, Canada, 2019.

[8] C. Pezerat, Q. Leclere, E. Le Roux, and J.-H. Thomas. Adapting the correction for CFAT application in time domain. In *Proceedings of Forum Acusticum*, Lyon, France, 2020.

[9] D. Bernal and A. Ussia. Sequential deconvolution input reconstruction. *Mechanical Systems and Signal Processing*, 50-51:41–55, 2015.

[10] A. N. Tikhonov. Solution of incorrectly formulated problems and the regularization method. *Soviet Mathematics*, 4:1035–1038, 1963.

[11] R. E. Kalman. A new approach to linear filtering and prediction problems. *Transactions of the ASME - Journal of Basic Engineering*, 82:35–45, 1960.

[12] A. Tarantola. *Inverse problem theory and methods for model parameter estimation.* SIAM Philadelphia, 2005.

[13] S. Särkkä. *Bayesian filtering and smoothing.* Cambridge University Press, 2013.

[14] E. Lourens, E. Reynders, G. De Roeck, G. Degrande, and G. Lombaert. An augmented kalman filter for force identification in structural dynamics. *Mechanical Systems and Signal Processing*, 27:446–460, 2012.

[15] R. Nayek, S. Chakraborty, and S. Narasimhan. A gaussian latent force model for joint input-state estimation in linear structural systems. *Mechanical Systems and Signal Processing*, 128:497–530, 2019.

[16] Joanna Zou, Eliz-Mari Lourens, and Alice Cicirello. Virtual sensing of subsoil strain response in monopile-based offshore wind turbines via gaussian process latent force models. *Mechanical Systems and Signal Processing*, 200:110488, 2023.

[17] S. Gillijns and B. De Moor. Unbiased minimum-variance input and state estimation for linear discrete-time systems with direct feedthrough. *Automatica*, 43:934–937, 2007.

[18] E. Lourens, C. Papadimitriou, S. Gillijns, E. Reynders, G. De Roeck, and G. Lombaert. Joint input-response estimation for structural systems based on reduced-order models and vibration data from a limited number of sensors. *Mechanical Systems and Signal Processing*, 29:310–327, 2012.

[19] O. Sedehi, C. Papadimitriou, D. Teymouri, and L. S. Katafygiotis. Sequential bayesian estimation of state and input in dynamical systems using output-only measurements. *Mechanical Systems and Signal Processing*, 131:659–688, 2019.

[20] S. Eftekhar Azam, E. Chatzi, and C. Papadimitriou. A dual kalman filter approach for state estimation via output-only acceleration measurements. *Mechanical Systems and Signal Processing*, 60-61:866–886, 2015.

[21] J. Ghibaudo, M. Aucejo, and O. De Smet. A sparse adaptive bayesian filter for input estimation problems. *Mechanical Systems and Signal Processing*, 180:109416, 2022.

[22] J. N. Yang, S. Pan, and H. Huang. An adaptive extended kalman filter for structural damage identifications ii: unknown inputs. *Structural Control and Health Monitoring*, 14:497–521, 2007.

[23] Z. Wan, T. Wang, L. Li, and Z. Xu. A novel coupled state/input/parameter identification method for linear structural systems. *Shock and Vibration*, 2018:7691721, 2018.

[24] K. Huang, K.-V. Yuen, and L. Wang. Real-time simultaneous input-state-parameter estimation with modulated colored noise excitation. *Mechanical Systems and Signal Processing*, 165:108378, 2022.

[25] D. Teymouri, O. Sedehi, L. S. Katafygiotis, and C. Papadimitriou. Input-state-parameter-noise identification and virtual sensing in dynamical systems: A bayesian expectation-maximization (bem) perspective. *Mechanical Systems and Signal Processing*, 185:109758, 2023.

[26] V.K. Dertimanis, E. N. Chatzi, S. Eftekhar Azam, and C. Papadimitriou. Input-state-parameter estimation of structural systems from limited output information. *Mechanical Systems and Signal Processing*, 126:711–746, 2019.

[27] M. Impraimakis and A. W. Smyth. An unscented kalman filter method for real time input-parameter-state estimation. *Mechanical Systems and Signal Processing*, 162:108026, 2022.

[28] M. Aucejo and Olivier de Smet. An optimal bayesian regularization for force reconstruction problems. *Mechanical Systems and Signal Processing*, 126:98–115, 2019.

[29] M. Aucejo and O. de Smet. On a full bayesian inference for force reconstruction problems. *Mechanical Systems and Signal Processing*, 104:36–59, 2018.

[30] K. Maes, E. Lourens, K. Van Nimmen, E. Reynders, G. De Roeck, and G. Lombaert. Design of sensor networks for instantaneous inversion

of modally reduced order models in structural dynamics. *Mechanical Systems and Signal Processing*, 52-53:628–644, 2015.

[31] M. Aucejo, Olivier de Smet, and J.-F. Deü. On a space-time regularization for force reconstruction problems. *Mechanical Systems and Signal Processing*, 118:549–567, 2019.

[32] D. Bernal. The zero-order hold in time domain identification: An unnecessary operating premise. *Structural Control and Health Monitoring*, 18(5):510–518, 2010.

[33] Daniz Teymouri, Omid Sedehi, Lambros S. Katafygiotis, and Costas Papadimitriou. A bayesian expectation-maximization (BEM) methodology for joint input-state estimation and virtual sensing of structures. *Mechanical Systems and Signal Processing*, 169:108602, apr 2022.

[34] S. Vettori, E. Di Lorenzo, B. Peeters, M.M. Luczak, and E. Chatzi. An adaptive-noise augmented kalman filter approach for input-state estimation in structural dynamics. *Mechanical Systems and Signal Processing*, 184:109654, 2023.

[35] O. W. Pertersen, O. Oiseth, T. S. Nord, and E. Lourens. Estimation of the full-field dynamic response of a floating bridge using kalman-type filtering algorithms. *Mechanical Systems and Signal Processing*, 107:12–28, 2018.

[36] M. Aucejo, O. De Smet, and J.-F. Deü. Practical issues on the applicability of kalman filtering for reconstructing mechanical sources in structural dynamics. *Journal of Sound and Vibration*, 442:45–70, 2019.